

Article

Biosynthesis of Gold- and Silver-Incorporated Carbon-Based Zinc Oxide Nanocomposites for the Photodegradation of Textile Dyes and Various Pharmaceuticals

Dineo A. Bopape^{1,2}, David E. Motaung³ and Nomso C. Hintsho-Mbita^{1,*} 

¹ Department of Chemistry, DSI/NRF Centre of Excellence in Strong Materials, University of Limpopo, Sovenga 0727, South Africa

² Department of Mathematics, Science and Technology Education (DMSTE), University of Limpopo, Sovenga 0727, South Africa

³ Department of Physics, University of the Free State, Bloemfontein 9300, South Africa

* Correspondence: nomso.hintsho-mbita@ul.ac.za

Abstract: Wastewater contaminated with dyes from the textile industry has been at the forefront in the last few decades, thus, it is imperative to find treatment methods that are safe and efficient. In this study, *C. benghalensis* plant extracts were used to synthesise by mass 20 mg/80 mg zinc oxide–carbon spheres (20/80 ZnO–CSs) nanocomposites, and the incorporation of the nanocomposites with 1% silver (1% Ag–ZnO–CSs) and 1% gold (1% Au–ZnO–CSs) was conducted. The impact of Ag and Au dopants on the morphological, optical, and photocatalytic properties of these nanocomposites in comparison to 20/80 ZnO–CSs was investigated. TEM, XRD, UV-vis, FTIR, TGA, and BET revealed various properties for these nanocomposites. TEM analysis revealed spherical particles with size distributions of 40–80 nm, 50–200 nm, and 50–250 nm for 1% Ag–ZnO–CSs, 1% Au–ZnO–CSs, and 20/80 ZnO–CSs, respectively. XRD data showed peaks corresponding to Ag, Au, ZnO, and CSs in all nanocomposites. TGA analysis reported a highly thermally stable material in ZnO-CS. The photocatalytic testing showed the 1% Au–ZnO–CSs to be the most efficient catalyst with a 98% degradation for MB textile dye. Moreover, 1% Au–ZnO–CSs also exhibited high degradation percentages for various pharmaceuticals. The material could not be reused and the trapping studies demonstrated that both OH• radicals and the e⁻ play a crucial role in the degradation of the MB. The photocatalyst in this study demonstrated effectiveness and high flexibility in degrading diverse contaminants.

Keywords: textile dyes; green synthesis; photocatalysts; antibiotics



Citation: Bopape, D.A.; Motaung, D.E.; Hintsho-Mbita, N.C. Biosynthesis of Gold- and Silver-Incorporated Carbon-Based Zinc Oxide Nanocomposites for the Photodegradation of Textile Dyes and Various Pharmaceuticals. *Textiles* **2024**, *4*, 104–125. <https://doi.org/10.3390/textiles4010008>

Academic Editor: Marta Gmurek

Received: 18 December 2023

Revised: 11 February 2024

Accepted: 26 February 2024

Published: 5 March 2024



Copyright: © 2024 by the authors. Licensee MDPI, Basel, Switzerland. This article is an open access article distributed under the terms and conditions of the Creative Commons Attribution (CC BY) license (<https://creativecommons.org/licenses/by/4.0/>).

1. Introduction

Water pollution is recognised as one of the major global environmental challenges contributing to water scarcity in various nations worldwide [1,2]. Despite the availability of current water treatment techniques, the detection of additional contaminants, such as textile dyes and pharmaceutical drugs, has increased in natural water sources. This increase persists each year with the identification of new contaminants [3]. While water contains a diverse range of contaminants, biological, organic, and inorganic, the literature indicates that organic contaminants pose a more significant challenge due to their non-biodegradable nature [4–6]. The textile industry significantly contributes to environmental water contamination by releasing wastewater containing dyes [7,8]. Even in low concentrations, the existence of these dyes is evident and undesirable in water [9]. These organic contaminants can find their way into human consumption through polluted water sources or the food chain, posing mutagenic risks to humans and harmful effects on aquatic ecosystems [10,11].

Methylene blue (MB) is a cationic textile dye utilised for biological staining and colouring various materials such as paper, hair, cotton, and wool [12]. Originally formulated

by Caro et al. in 1876 for dyeing cotton in the textile industry, MB stands as one of the earliest synthetic dyestuffs [13,14]. It has been identified as a cationic dye categorised as a toxic colourant and has been associated with adverse effects [15]. The presence of methylene blue in wastewater can lead to health issues, including respiratory problems, vomiting, eye irritation, diarrhoea, and nausea [12]. Human exposure or ingestion of methylene blue may result in various symptoms, including mental disorders [14–17].

To address the removal of such contaminants from water streams, various methods have been employed, including chlorination, reverse osmosis, adsorption, and electrochemical degradation [18–24]. However, these methods often have limitations such as the generation of large quantities of sludge, by-product formation, high operational costs, and limited selectivity. Recently, photocatalysis has gained popularity as a highly recommended method for degrading diverse pollutants [25]. Photocatalysts like zinc oxide (ZnO), titanium dioxide (TiO₂), iron oxide (Fe₂O₃), etc. have proven successful at degrading contaminants in water [26–28]. ZnO was chosen for this study because it is highly efficient in degrading various pollutants, possesses numerous active sites, and exhibits effective radicals on its surfaces during the photodegradation process [29,30]. Nevertheless, ZnO exhibits a high recombination rate, limited surface area, and a wide bandgap measuring 3.2 eV [31–33]. Materials containing carbon are extensively utilised as adsorbents and serve as a foundation for incorporating inorganic nanomaterials to enhance mechanical and thermal stability, as well as to augment the adsorption capacity of metal oxides such as ZnO [34,35]. The motivation behind depositing metal oxide nanocomposites onto carbon nanomaterials of diverse shapes stems from numerous literature reports on carbon nanomaterials dating back to their discovery in 1991 by Iijima [36]. These carbon nanomaterials are recognised for their thermal stability, photoelectric properties (dots), and mesoporosity, resulting in a substantial surface area for the materials [37,38]. Additionally, noble metals were reported to slow the rate of e⁻/h⁺ recombination, while also broadening the absorption spectrum of metal oxides [39–42]. Silver (Ag) has been reported to be less expensive, easily doped, and to have high conductivity and light absorption capacity [43,44]. Gold (Au) has higher electron affinity, and it is known to collect photogenerated electrons during ZnO photoexcitation, increasing photocatalytic efficiency [45–47]. According to the literature, doping metal oxides with Ag and Au has increased the photocurrent response, ultraviolet and visible light photocatalytic activity, and photocatalytic efficiency [48–50].

Additionally, the preparation process for these ZnO nanomaterials often involves harmful reactants as reducing and capping agents, leading to impurities in the synthesised materials due to the addition of various chemical promoters [39,48]. Therefore, it is crucial to develop an eco-friendly and inexpensive method for preparing ZnO that avoids the use of harmful reactants. In this study, the synthesis of Ag/Au-ZnO-C was through an environmentally friendly route, using the *Commelina benghalensis* plant extract.

These methods are simple, not harmful to the environment, and cheap, replacing harmful reagents with natural reducing agents from plant extracts, bacteria, algae, etc. [39]. Biosynthesised metal oxides resulting from these methods have been reported to effectively degrade various pollutants. Various studies were conducted and Niu et al. [40] utilised Ag/ZnO@C-2 to demonstrate the highest efficiency in photodegrading RhB, achieving a ~98% degradation in 40 min under simulated sunlight. The photodegradation rate of Ag/ZnO@C-2 was almost ten times that of pure ZnO, providing quantitative evidence for its exceptional photocatalytic performance. In another study, Chen et al. [41] revealed a photodegradation efficiency of 87.4% for Orange II dye while utilising the of Au/C-ZnO photocatalyst, surpassing the corresponding degradation of 82.1% by the C-ZnO photocatalyst. These studies highlight the effect of carbon and Ag in trapping and increasing the surface area, facilitating more active sites on the material. Therefore, the objective of this study was to dope environmentally friendly C-ZnO materials with noble metals for treating wastewater effluents to acceptable levels for both animal and human health. Therefore, the 20/80 ZnO-CSs was doped with optimised 1% Ag and 1% Au separately and then their efficiency was tested against MB textile dye and various pharmaceutical pollutants.

2. Experimental

2.1. Chemicals and Materials

All the chemicals employed in this study were of analytical grade and were used in their original state. The *C. benghalensis* plant was sourced from the University of Limpopo field, subsequently dried, and ground at the Chemistry Department of the University of Limpopo. Zinc nitrate hexahydrate ($\text{Zn}(\text{NO}_3)_2 \cdot 6\text{H}_2\text{O}$), orthophosphoric acid (H_3PO_4), Silver nitrate (AgNO_3) and Gold (III) chloride trihydrate ($\text{HAuCl}_4 \cdot 3\text{H}_2\text{O}$) were procured from Sigma Aldrich, Darmstadt, Germany. Sucrose ($\text{C}_{12}\text{H}_{22}\text{O}_{11}$), Sulfamethoxazole (SMX), Ciprofloxacin (CIP), and Carbamazepine (CBZ) were all purchased at Protea Labs, Midrand, South Africa. Sulfisoxazole (SSX) and methylene blue (MB) were acquired from the University of Limpopo's Department of Chemistry Chemical Store Room.

2.2. Preparation of Plant Extracts

The *Commelina benghalensis* (*C. benghalensis*) plant extracts were prepared utilising the tea infusion method [42]. A quantity of 10 g of crushed *C. benghalensis* powder was measured and placed in a 500 mL conical flask with 250 mL of boiling deionised water. The mixture was heated at 80 °C for 15 min until a green-brownish colour emerged. Following cooling to room temperature, the *C. benghalensis* extract was obtained through vacuum filtration using Munktell filter paper with a 45 mm diameter. The resultant extracts were stored in a refrigerator at 4 °C for subsequent characterisation and application.

2.3. Phytochemical Characterisations Using the LC-MS Technique

The identification of various chemical groups within *C. benghalensis* extracts was conducted using a Sciex S500r quadrupole time-of-flight (QTOF) mass spectrometer connected to an Exion LC liquid chromatography instrument. A 10 mL aliquot of the extract was introduced into the instrument via an autosampler. Chromatographic analysis involved a C_{18} column (Phenomenex, 100 mm \times 2 mm) with separation conditions comprising a mobile phase of (i) water/formic acid 0.1% (v/v) and (ii) methanol/water containing 0.1% (v/v) formic acid, with a flow rate of 1 mL/min and gradients of 0–1.0 min/2% (v/v), 1–10 min/2–80% (v/v), 10–12 min/80% (v/v), 12–13 min/80–2% (v/v). For estimation, multiple reaction monitoring (MRM) in positive mode with a scan time of 50 min was employed. The first transition served for quantification, and the second for confirmation, utilising the equation (Equation (1)):

$$Y = 6.653e + 004x + 7.856 + 003 \quad (r = 0.9946) \quad (1)$$

2.4. *C. benghalensis*-Mediated ZnO Nanoparticle Synthesis

The eco-friendly synthesis of ZnO-NPs commenced with the measurement of 4 g of $\text{Zn}(\text{NO}_3)_2 \cdot 6\text{H}_2\text{O}$ salt, which was added to 250 mL conical flasks according to the procedure outlined by Munyai et al. [43]. Subsequently, 50 mL of the plant extract was introduced into each flask containing the Zn salt, resulting in a brownish-yellowish solution. The mixture was then boiled for an hour, followed by cooling to room temperature, transferred to a crucible, and overnight heating in an oven at 80 °C. The resulting product was washed with deionised water, filtered using a membrane filtration system, subjected to calcination at 700 °C for 2 h, and subsequently collected, crushed, and stored for subsequent analysis.

2.5. Preparation of Carbon Spheres (CSs)

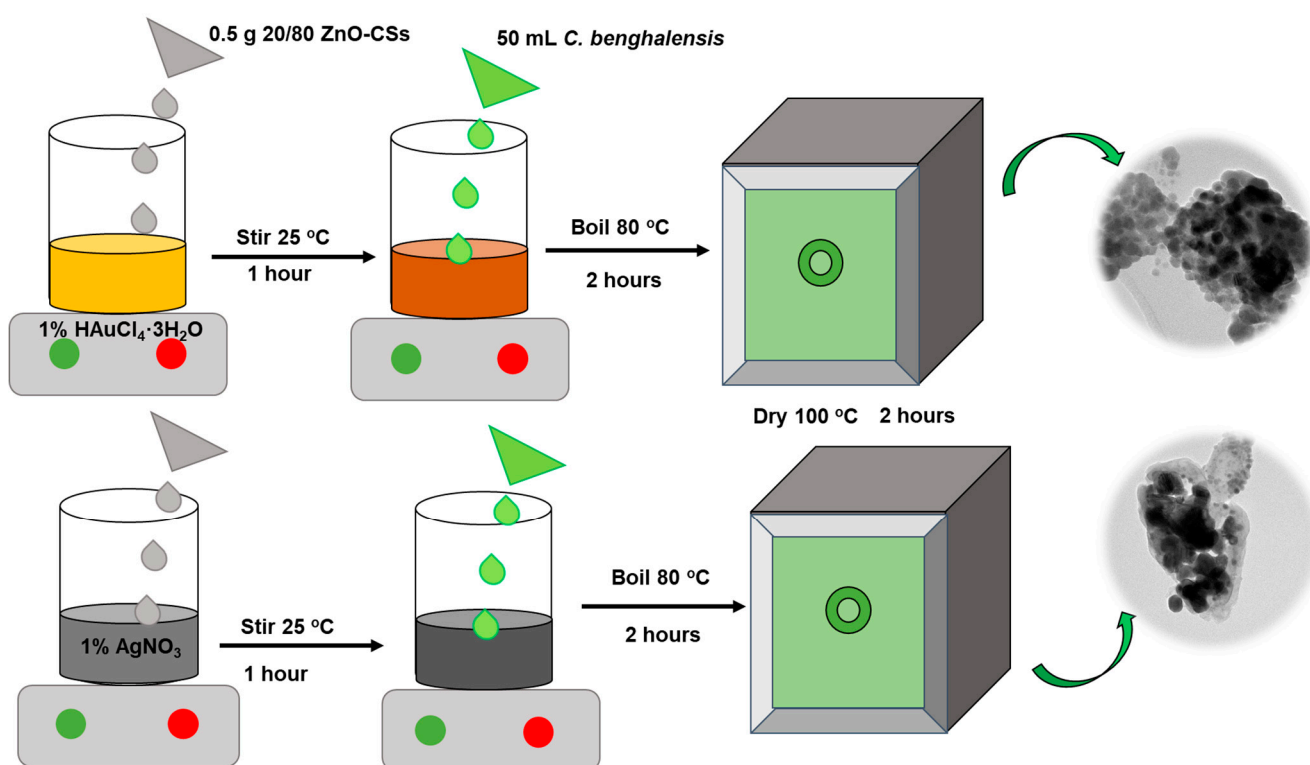
For the production of carbon spheres (CSs), 2 g of sucrose was dissolved in 10 mL of deionised water, and then 20 mL of orthophosphoric acid was added. The resulting mixture underwent microwaving (1000 W) for three minutes. The resulting black product was subjected to five cycles of centrifugation at 4000 rpm for five minutes each, followed by drying in an oven at 80 °C. The resultant carbon was subsequently crushed for subsequent use and characterisations [44].

2.6. Preparation of Carbon Spheres-Incorporated (ZnO–CSs) Nanocomposites

The preparation of 20/80 (ZnO–CSs) nanocomposites utilised the ultrasonication method [45]. Initially, as-prepared ZnO-NPs (20 mg) were separately combined with carbon spheres (80 mg). These mixtures were then dispersed in 100 mL of distilled water, and the resulting dispersions underwent ultrasonic treatment for 1 h to achieve a uniform suspension of 20/80 ZnO–CSs. The resultant suspensions were subsequently filtered, washed with distilled water, and dried in an oven at 100 °C for 12 h. The materials were stored for subsequent analysis and characterisation.

2.7. Preparation of Metal-Doped ZnO–CSs Composites

Initially, 0.5 g of 20/80 ZnO–CSs was added to 50 mL of 1% AgNO₃ solution and 1% HAuCl₄·3H₂O solution separately. The solutions were magnetically stirred for 1 h, followed by the addition of 50 mL of *C. benghalensis* extract to each solution, and heating up to 80 °C for 2 h as shown in Scheme 1 [46]. The resulting product was washed and further dried in a vacuum oven at 100 °C for 2 h, and stored for further characterisation and investigation.



Scheme 1. Green synthesis of 1% Ag–ZnO–CSs and 1% Au–ZnO–CSs using *C. benghalensis* plant extract.

2.8. Analysis of Materials

To evaluate the optical properties and dye substance concentration of the synthesised materials, an Agilent Cary 100 UV–Vis Varian spectrophotometer was employed. Samples were placed in a 10 mm path length cuvette, and 5 mL were withdrawn at regular intervals for spectral analysis. The crystallinity and phase composition were determined using a Bruker AXS D8 Advance X-ray Diffractometer (Germany), scanning in the range of 20–90 2θ degrees over a 2 h period. Transmission electron microscopy (TEM) was utilised to analyse the morphology and particle size of the samples. Electron dispersive X-ray analysis (EDX) was conducted for elemental and chemical analysis. The Bruner–Emmet–Teller (BET) surface analyser was used at 196 °C to measure pore sizes, surface area, and pore volume, with the sample heated to 150 °C for 2 h under N₂ gas flow. For the thermal stability

assessment, a Perkin Elmer Pyris Thermogravimetric Analyser (TGA) was employed, heating approximately 0.01 g of the material at a rate of 10 °C/min up to 900 °C.

2.9. Photocatalytic Decomposition of MB Dye

Firstly, optimisation experiments were explored using the 20/80 ZnO–CSs photocatalyst (Section S1). The optimum pH of 5, photocatalyst dosage of 90 mg, and concentration of 5 ppm (MB) were utilised for all the photocatalytic studies (20/80 ZnO–CSs, 1% Ag–ZnO–CSs and 1% Au–ZnO–CSs) of the current work. In a typical photocatalytic experiment, about 300 mL of a 5 ppm methylene blue (MB) solution at pH 5 was combined with 90 mg of photocatalyst (20/80 ZnO–CSs). Then, 1% Ag–ZnO–CSs and 1% Au–ZnO–CSs powder were transferred to a photochemical reactor. The mixture was stirred in the absence of light for approximately 30 min to attain adsorption–desorption equilibrium. Following this, the solution was subjected to UV light (450 W) for a duration of 2 h, with samples collected at 30 min intervals for analysis using a UV-vis spectrophotometer. The progress of degradation was monitored by measuring the absorbance at the maximum wavelength of 665 nm for MB. The degradation efficiency was then calculated using the formula:

$$\% \text{ Degradation} = \left(\frac{A_0 - A_f}{A_0} \right) \times 100 \quad (2)$$

where A_0 = is the initial absorbance at 0 min (adsorption–desorption), A_f = is the final absorbance 30, 60, 90, and 120 min of photodegradation

2.9.1. Reusability

In order to evaluate the robustness and reusability of the 1% Au–ZnO–CSs nanocomposite, four recycling trials were conducted under conditions similar to those utilised in standard photocatalytic degradation trials. Following each cycle, the photocatalyst was thoroughly washed with distilled water and was recovered through membrane filtration. Afterwards, the material was dried at 60 °C to obtain a powder for the following cycle.

2.9.2. Trapping Studies

In the course of photodegradation of MB dye, 2 mL (5 mmol) each of EDTA, isopropyl alcohol, silver nitrate, and p-benzoquinone were introduced to capture holes (h^+), hydroxyl radicals (OH^\bullet), electrons (e^-), and superoxide (O_2^{2-}), respectively. The photodegradation conditions employed were similar to those applied in standard photocatalytic degradation assessments.

2.10. Photocatalytic Degradation of Pharmaceuticals

For the degradation of SSX/SMX/CIP/CBZ pharmaceuticals, 90 mg of photocatalyst was introduced into a 300 mL solution with a concentration of 5 ppm (pH 5). Before UV exposure, the solution underwent stirring for 30 min to establish adsorption–desorption equilibrium. The photodegradation process extended over 2 h, and samples were collected at 0, 30, 60, 90, and 120 min. The residual concentrations of SSX/SMX/CIP/CBZ were analysed using a UV/vis spectrophotometer at $\lambda_{\max} = 275\text{--}290$ nm. The degradation efficiency was then calculated using the formula:

$$\% \text{ degradation} = 100 \left(\frac{A_0 - A_f}{A_0} \right) \quad (3)$$

where A_0 = the initial absorbance (before photodegradation) of SSX/SMX/CIP and CBZ at $\lambda_{\max} = 290/280/285$ and 290 nm, A_f = is the final absorbance after photodegradation/adsorption.

3. Results and Discussion

3.1. Plant Extract Analysis by LC-MS

The molecular weights of components within the *C. benghalensis* extract were determined through LC-MS analysis. The examination identified the existence of eleven potential compounds in the plant extract, as outlined in Table 1.

Table 1. Liquid chromatography mass spectrometry (LCMS) results for *C. benghalensis* plant extract.

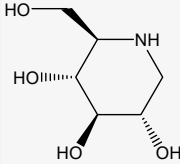
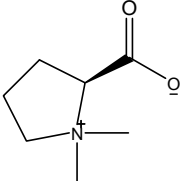
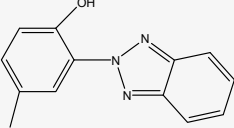
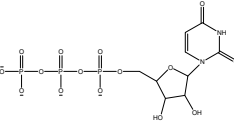
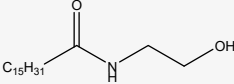
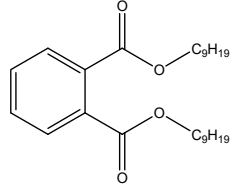
Molecular Mass	Name of Molecule	Biomolecule Group	Structure	Molecular Formula
164.093	1-Deoxynojirimycin	Alkaloids		C ₇ H ₉ N ₅
144.102	Stachydrine	Amino acids		C ₇ H ₁₃ NO ₂
226.097	2-(2-Hydroxy-5-methylphenyl)benzotriaz	Phenols		C ₂ H ₁₁ N ₉ O ₄
405.175	Uridine 5-diphosphate	Sugars		C ₁₈ H ₂₈ O ₁₀
256.264	Palmitamide	Fatty acids		C ₁₆ H ₃₃ NO
419.317	Di(5-nonyl) phthalate	Carboxylic acids		C ₂₇ H ₃₈ N ₄

Table 1 presents a summary of the LC-MS data regarding some of the potential compounds identified in *C. benghalensis* plant extracts. The LC-MS analysis revealed the presence of compounds such as alkaloids, esters, phenols, carboxylic acids, etc. The mass-to-charge ratio (m/z) derived from the coupled LC-MS data were utilised to generate the potential organic structures detailed in the Table 1. The data highlight the elevated presence of OH groups in *C. benghalensis* plant extracts, primarily originating from alkaloids, carboxylic acids, and polyphenols. Additionally, in our previous study [47], we performed qualitative tests on the *C. benghalensis* plant extracts, and the presence of terpenoids, glycosides, phenols, alkaloids, tannins, phlobatannins, and anthraquinones was reported. These constituents exhibit biological activity and have the potential to assist in the treatment of various water pollutants. For example, Mallikarjunaswamy et al. [1] reported that the presence of terpenoids and phenolic compounds on Indian bael fruits-mediated ZnO played roles of both antioxidants and reducing agents. Suresh et al. [5] reported on *Cassia fistula* plant extract-mediated ZnO nanomaterials. The analysis revealed that the extract contained reducing and antioxidant agents, notably polyphenols (11%) and

flavonoids (12.5%). Interestingly, Sharma et al. [6] synthesised *Ficus palmate*-mediated ZnO nanomaterials, which exhibited better antioxidant and antibacterial activity as compared to the *Ficus palmate* plant extract.

3.2. Structural Analysis

Figure 1a,b illustrates the XRD patterns for 20/80 ZnO-CSs, 1% Ag-ZnO-CSs, and 1% Au-ZnO-CSs. The diffractogram of 1% Ag-ZnO-CSs exhibits distinctive peaks at 32.20° , 37.9° , 43.9° , 54.1° , 64.9° , 77.3° , and 81.6° , corresponding to the (1 0 0), (1 1 1), (2 0 0), (0 0 4), (2 2 0), (3 1 1), and (2 2 2) planes, respectively [48–50]. The broad peaks around 21.60° and 43.5° correspond to carbon sphere (002) and (1 0 0) planes, respectively [51]. In comparison to the standard peak values of ZnO (JCPDS No.36-1451) [50], the ZnO nanocomposite exhibits a hexagonal wurtzite structure, with the (1 0 0) and (1 1 1) planes reported in this study, consistent with data obtained by Yu et al. [52]. Du et al. [53] reported similar findings, with the broad peak for CSs at around 21° . The XRD pattern (Figure 1a) indicates that the ZnO peaks are more visible in 1% Ag-ZnO-CSs compared to 1% Au-ZnO-CSs and 20/80 ZnO-CSs, while the CSs peak remains constant. Additional peaks appear at 30.5° , 37.9° , 43.9° , 54.1° , 64.9° , 77.3° , and 81.6° , corresponding to lattice planes (1 0 0), (0 0 2), (1 1 1), (2 0 0), (0 0 4), (2 2 0), (3 1 1), and (2 2 2), respectively. The presence of the Ag (1 1 1) peak in XRD patterns further supports the formation of metallic silver. The absence of a shift in the peak position for the 1% Ag-ZnO-CSs sample indicates that Ag particles are situated on the surfaces of ZnO nanoparticles, ruling out the possibility of Ag particles entering the ZnO lattice or substituting Zn sites [54].

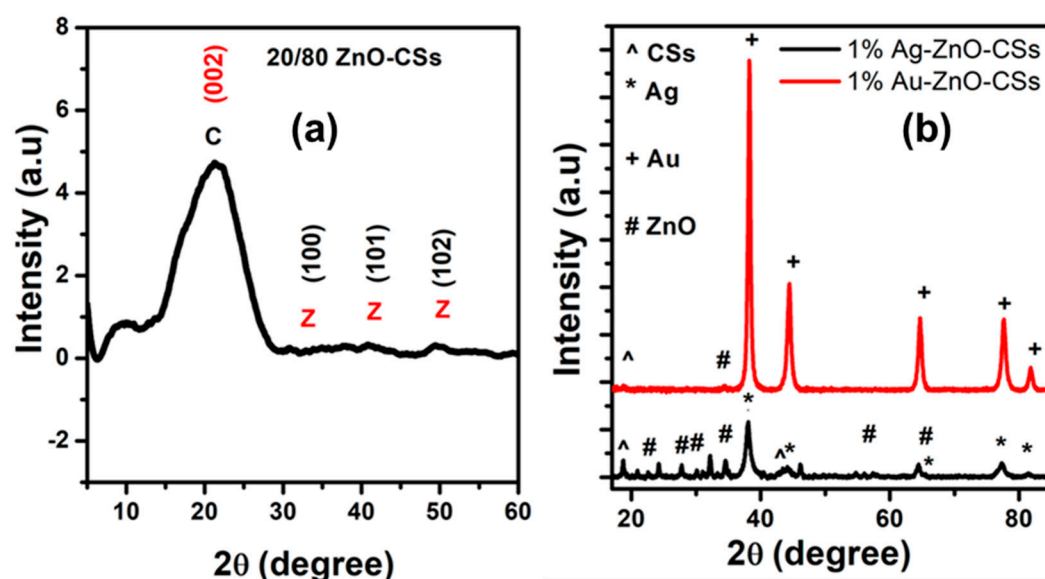


Figure 1. XRD patterns for (a) 20/80 ZnO-CSs, (b) 1% Ag-ZnO-CSs and 1% Au-ZnO-CSs.

The diffractogram of 1% Au-ZnO-CSs displays strong peaks at 38.50° , 37.9° , 43.3° , 64.5° , 77.3° , and 81.3° , corresponding to the (1 1 1), (2 0 0), (2 2 0), (3 1 1), and (2 2 2) planes of face-centered cubic gold (JCPDS No. 65-8601) [55–57]. The crystallite sizes for 1% Ag-ZnO-CSs and 1% Au-ZnO-CSs were measured at 15.9 and 5.4 nm, respectively. Notably, the data reveal a significant phase transformation in CSs, evident in the 20/80 ZnO-CSs XRD diffractogram, which exhibits a broad peak aligned with the 002 plane of carbon, signifying an amorphous phase. In contrast, the 1% Ag-ZnO-CSs and 1% Au-ZnO-CSs nanocomposites exhibit a more crystalline peak on the same plane for CSs material, suggesting an impact of the doping procedure involving high-temperature conditions [56]. Intriguingly, the peaks associated with noble metals (Ag and Au) are more pronounced and well-defined compared to those of ZnO and CSs in the 1% Ag-ZnO-CSs and Au-ZnO-CSs, indicating the successful doping of these metals onto the ZnO-CSs [55].

3.3. Optical Properties

To gather insights into the optical characteristics of these materials, Figure 2a,b illustrates the UV-DRS analyses of the 20/80 ZnO-CSs, 1% Ag-ZnO-CSs, and 1% Au-ZnO-CSs, with Tauc's plots employed for interpretation. In the spectrum, the 20/80 ZnO-CSs nanocomposites exhibit absorption bands at approximately 301 nm and 287 nm, attributed to ZnO and CSs, respectively. The 1% Ag-ZnO-CSs display absorption bands at 298 nm and 286 nm, corresponding to the absorption peaks of Ag and ZnO-CSs, respectively [58–60]. The presence of Ag induces a blue-shift in the absorbance spectrum, with the maximum absorbance peak for Ag-ZnO-CSs at 298 nm instead of ~301 nm. The surface Plasmon band of the 1% Ag-ZnO-CSs composite exhibits a distinctive broadening attributed to robust interfacial electronic coupling between adjacent ZnO and Ag nanoparticles [61]. This Plasmon oscillation has the potential to amplify light scattering by facilitating the interaction between incident light and Ag nanoparticles. Consequently, this extends the optical path, contributing to a reduction in light energy loss. Previous studies have reported an absorbance band at 379 nm, corresponding to the ZnO absorption peak, and the Ag NPs peak at 402 nm [58].

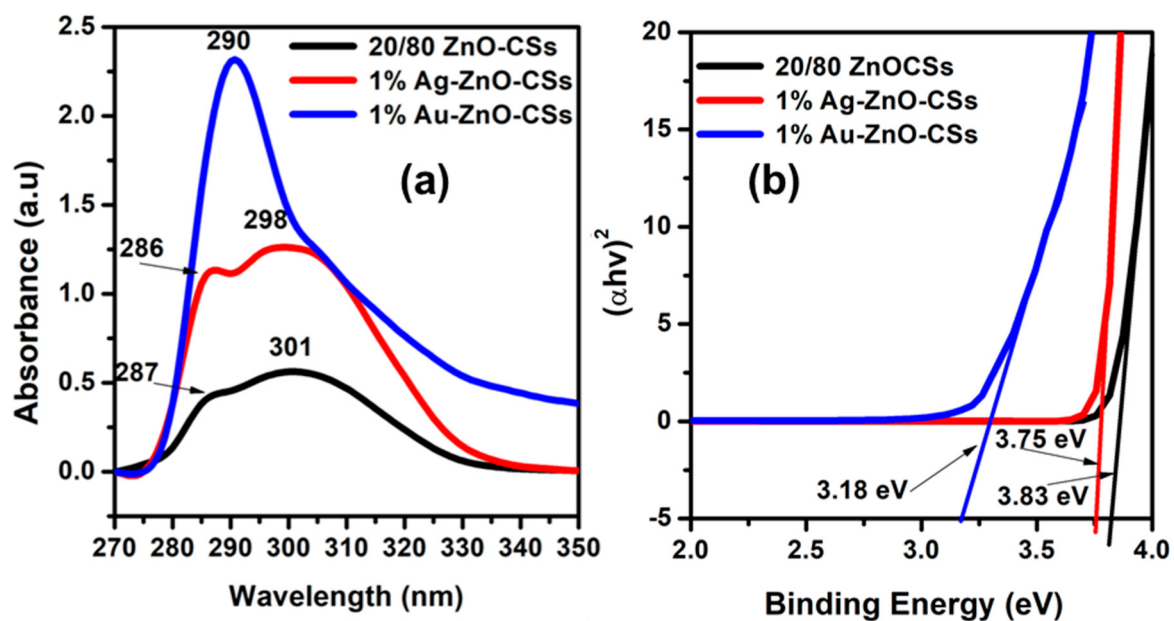


Figure 2. (a) UV-Vis curves for 20/80 ZnO-CSs, 1% Ag-ZnO-CSs and 1% Au-ZnO-CSs and the corresponding (b) Tauc's plot.

The corresponding bandgap for 1% Ag-ZnO-CSs was determined to be 3.75 eV by extrapolating the linear region of Tauc's plot [62]. This value is slightly higher than the 3.33 eV bandgap reported by Kotlhao et al. [59]. The inconsistency can be attributed to the UV activity of the nanocomposites synthesised in this study, while those obtained by Kadam et al. [58] and Kotlhao et al. [59] were active in the visible region.

A band at approximately 290 nm was detected in the 1% Au-ZnO-CSs, confirming the presence of gold in the ZnO-CSs material [63,64]. The shift observed in the ZnO band position in the 1% Au-ZnO-CSs nanoparticles can be explained by the higher electronegativity of gold compared to silver. Gold's elevated electronegativity results in a stronger attraction of electron density towards itself, influencing the positional shift of the ZnO band [63]. However, the recorded absorption band was smaller than those documented in the literature. Fageria et al. [63] identified two bands at 378 nm and 560 nm, where the 378 nm position corresponds to ZnO presence, and the other band indicates the formation of gold nanoparticles. Gogurla et al. [64] reported two peaks—one in the UV region around 380 nm and another in the visible region around 550 nm. The UV peak is ascribed to

ZnO's band edge absorption, while the visible peak is attributed to the surface Plasmon absorption of gold nanoparticles. Liu et al. [65] observed a red-shift in two characteristic gold plasma resonance peaks from 522 to 530 nm for pure gold nanoparticles coated with ZnO nanopyramids, indicating the presence of gold nanoparticles surrounded by high-refractive-index ZnO shells.

The bandgap of 1% Au-ZnO-CSs was determined to be 3.79 eV, which is larger than the 3.12 eV bandgap reported by Fageria et al. [63]. Thi et al. [61] found a bandgap of 2.92 eV for Au/ZnO/GO, and Chang et al. [66] reported a bandgap of 3.02 eV for Au-ZnO-C. The presence of gold nanoparticles likely played a significant role in the optical properties of the materials, causing a shift to the lower UV region and higher bandgaps compared to materials active in the visible region, as reported by Fageria et al. [63] and Gogurla et al. [64].

3.4. TGA Analysis

Figure 3 illustrates the TGA curves for 20/80 ZnO-CSs, 1% Ag-ZnO-CSs, and 1% Au-ZnO-CSs. In the temperature range of 0 to 200 °C, both 1% Ag-ZnO-CSs and 1% Au-ZnO-CSs exhibit a gradual weight loss of 4.3% and 4.9%, respectively. This gradual weight loss suggests the evaporation of volatile substances and water from the samples [66,67]. The second stage of weight loss, occurring between 200 and 400 °C, accounts for approximately 20% of the total weight loss. This stage indicates the removal of hydroxyl groups within the structures of 1% Ag-ZnO-CSs and 1% Au-ZnO-CSs [68–71]. In the final stage, spanning from 400 to 900 °C, the total weight loss reaches 64.3% for 1% Ag-ZnO-CSs and 69.6% for 1% Au-ZnO-CSs. These findings suggest that 1% Ag-ZnO-CSs exhibits greater thermal stability than 1% Au-ZnO-CSs. Additionally, both materials show less stability than 20/80 ZnO-CSs, where the total weight percentages at 900 °C are approximately 54.2%, 36.4%, and 29.7% for 20/80 ZnO-CSs, 1% Ag-ZnO-CSs, and 1% Au-ZnO-CSs, respectively. These results align with those reported by Ramesan et al. [70], who observed a weight loss of 74.2% at 700 °C for Ag-doped ZnO-C material. The TGA curve of Au-decorated ZnO-PANI prepared by Bonyani et al. [72] showed a 25% weight loss from 0 to 700 °C, which is comparable to the findings in this study.

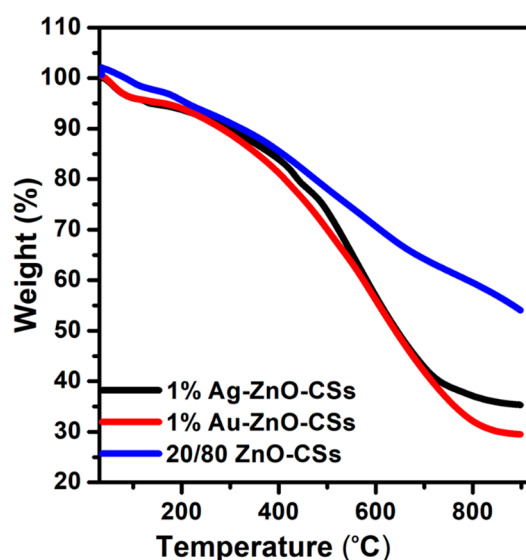


Figure 3. TGA diagrams for 20/80 ZnO-CSs, 1% Ag-ZnO-CSs, and 1% Au-ZnO-CSs.

3.5. Morphological and Elemental Analysis of Nanocomposites

The transmission electron microscope (TEM) technique can be used to verify the incorporation of 1% Ag-ZnO-CSs and 1% Au-ZnO-CSs. Figure 4a–i shows the TEM micrographs of the obtained 20/80 ZnO-CSs, 1% Ag-ZnO-CSs, and 1% Au-ZnO-CSs nanomaterials. The prepared 1% Ag-ZnO-CSs had spherically shaped particles with length

distributions ranging from 20 to 100 nm, with the most dominant particles ranging from 40 to 80 nm. While the prepared 1% Au–ZnO–CSs had spherically shaped particles with length distributions ranging from 50 to 400 nm, with the most dominant particles ranging from 50 to 250 nm. The particle sizes of the noble metal-doped nanocomposites were smaller 20/80 ZnO–CSs with particle size distributions between 50 and 250 nm. The 1% Ag–ZnO–CSs obtained in the study were almost the same size as the Ag–ZnO flowerlike nanostructures obtained by Patil et al. [73] which were 70 nm. The Au–ZnO obtained by Majhi et al. [57], were reported to be 100 nm.

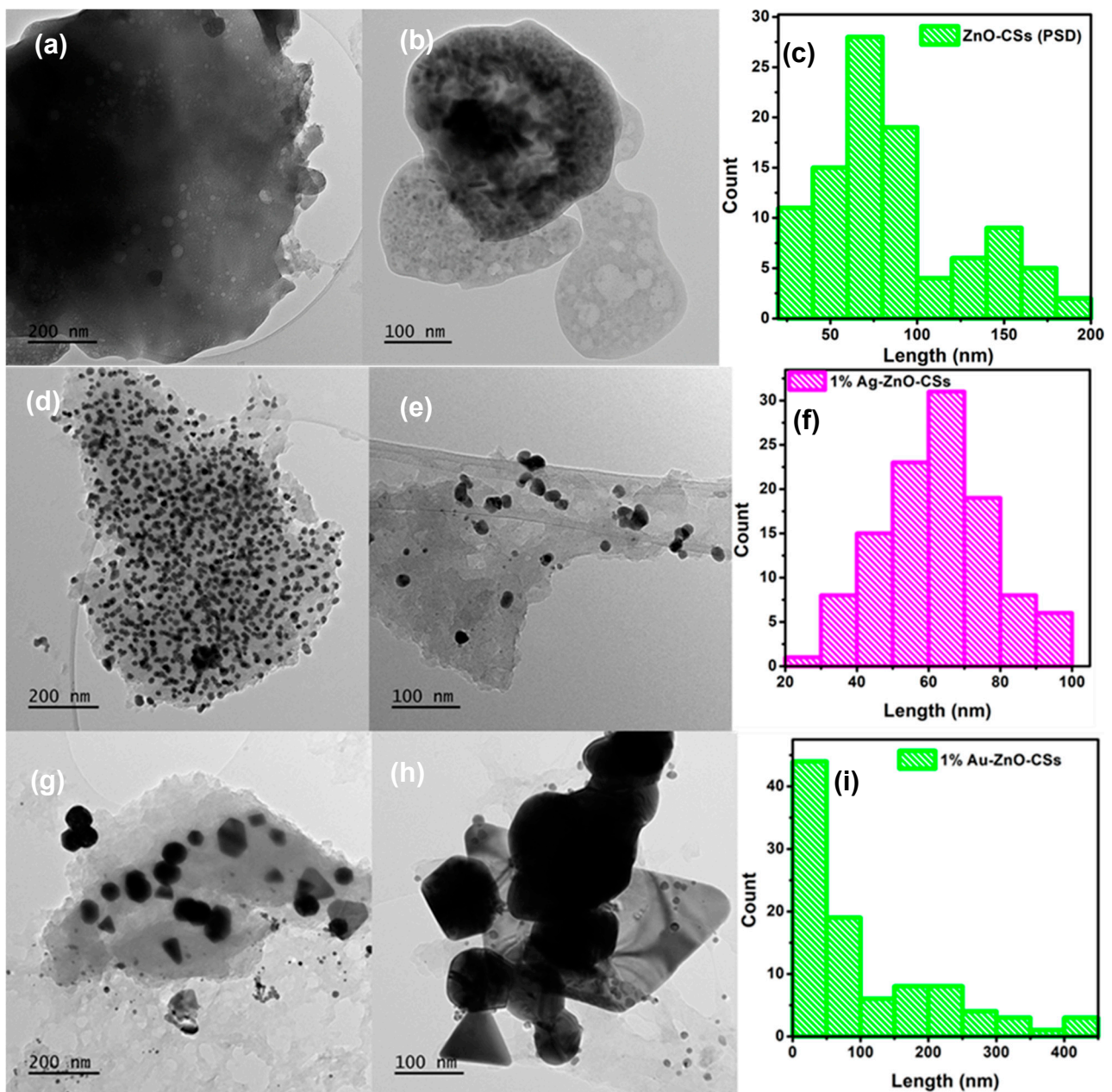


Figure 4. (a) Low- and (b) high-resolution TEM images of 20/80-ZnO–CSs and (c) the corresponding particle size distribution curve, (d) low- and (e) high-resolution TEM images of 1% Ag–ZnO–CSs and (f) the corresponding particle size distribution curve, (g) low- and (h) high-resolution TEM images of 1% Au–ZnO–CSs and (i) the corresponding particle size distribution curve.

To further confirm the deposition of the noble metals, EDS was also conducted (see Figure S1). There was indeed a successful deposition of Au and Ag in the nanomaterials.

3.6. N₂ Adsorption–Desorption Studies, BJH Pore Volume, and BET Surface Area

The analysis of N₂ adsorption–desorption was conducted to explore the impact of noble metal incorporation on the surface area and porosity of the ZnO–CSs. The Brunauer–Emmett–Teller (BET) method was employed for specific surface area calculations. Figure 5a illustrates the N₂ adsorption–desorption isotherm, while Figure 5b displays the BJH pore size distribution curves, and Figure 5c presents the BET surface area curves for the 20/80 ZnO–CSs, 1% Ag–ZnO–CSs, and 1% Au–ZnO–CSs. The BET surface area values (Figure 5c) were 21.95 m²/g, 10.799 m²/g, and 20.106 m²/g for 1% Ag–ZnO–CSs, 1% Au–ZnO–CSs, and 20/80 ZnO–CSs, respectively. The adsorption–desorption isotherms of 1% Ag–ZnO–CSs (Figure 5a) can be categorised as a typical type IV isotherm with a hysteresis loop H3 in accordance with IUPAC nomenclature, indicating a purely mesoporous material with small pore sizes [74–76]. The isotherms for 1% Au–ZnO–CSs and 20/80 ZnO–CSs exhibited hysteresis loops of type H2 (Figure 5a), indicating a mixture of macropores and mesopores [77,78]. Figure 5b depicts the pore size distribution measured by the BJH (Barrett–Joyner–Halenda) desorption hysteresis loop. The type IV hysteresis loop of the adsorption–desorption curves suggests the presence of mesoporous particles, even at high relative pressures (P/P₀), with a hysteresis loop showing decreasing adsorption and a moderately sharp desorption branch [76].

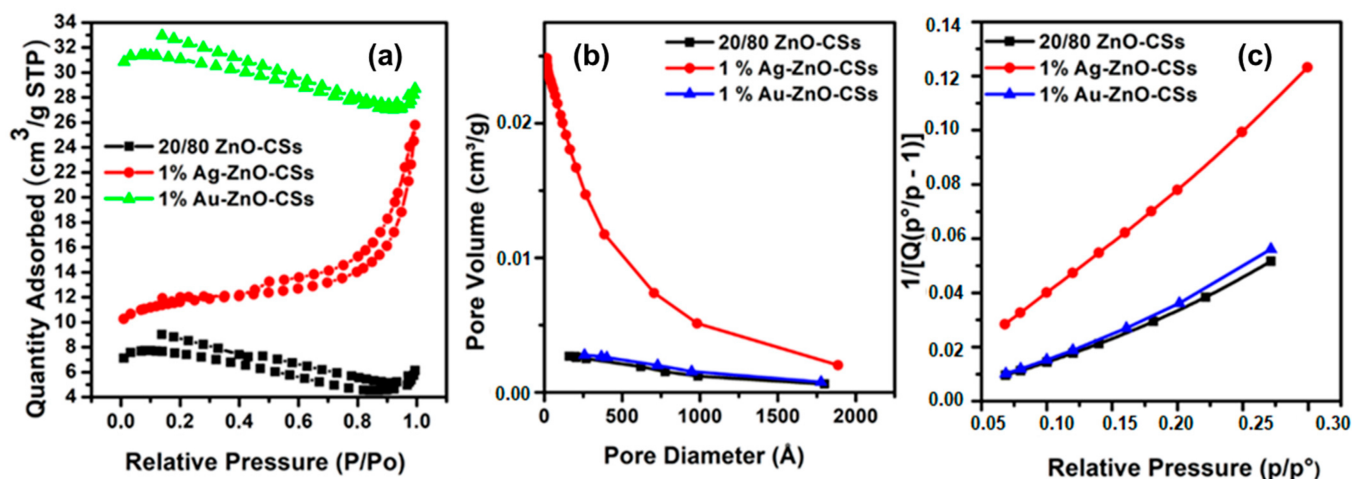
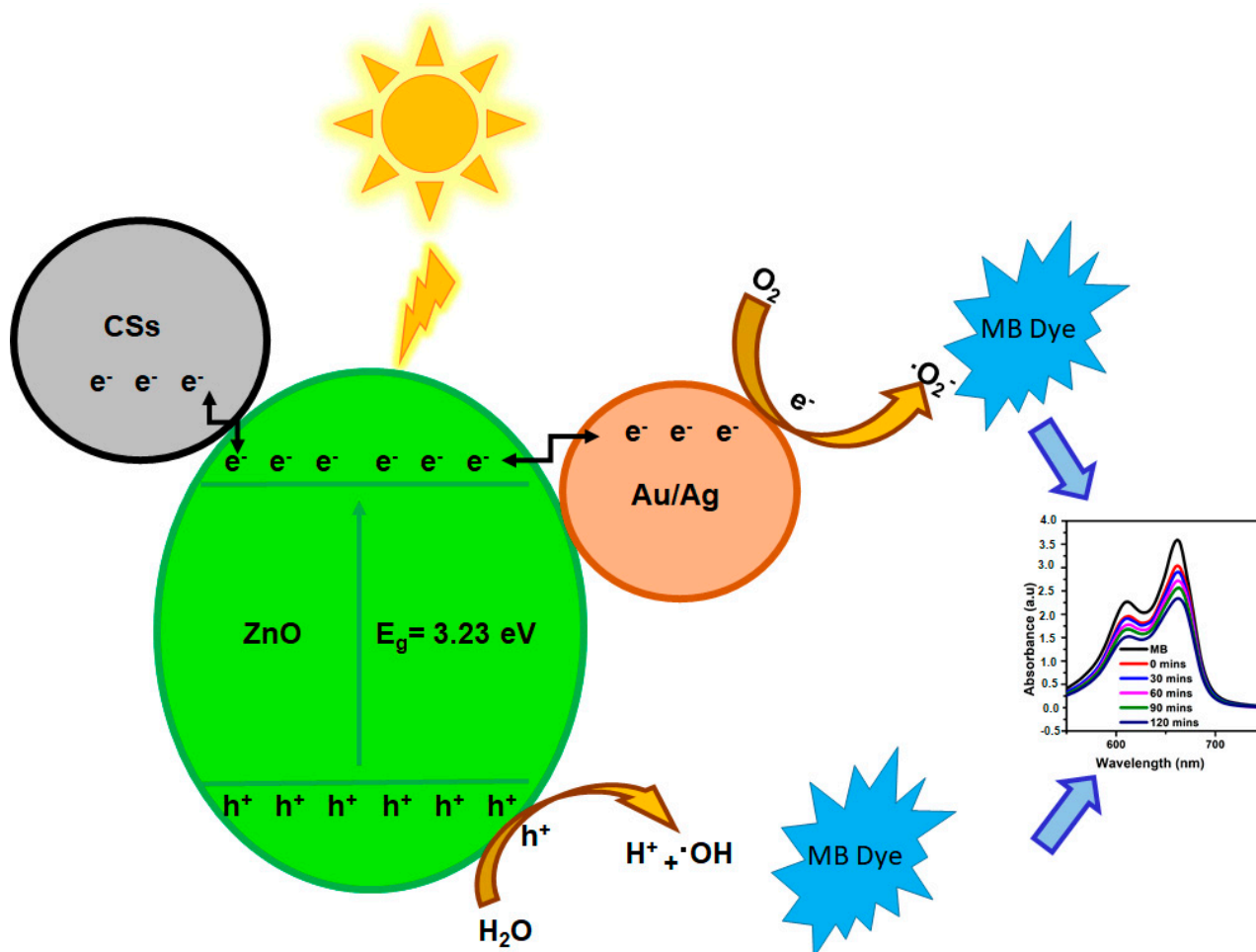


Figure 5. The 20/80 ZnO–CSs, 1% Ag–ZnO–CSs, and 1% Au–ZnO–CSs adsorption–desorption isotherms (a) with the pore volume distribution curve (b,c) the surface area diagram.

3.7. Photodegradation Studies

To investigate whether the deposition of noble metals on ZnO–CSs enhances dye degradation, analyses of UV-vis photodegradation curves were conducted. In the proposed degradation mechanism depicted in Scheme 2, when light interacts with 1% Ag–ZnO–CSs and 1% Au–ZnO–CSs, two simultaneous reactions occur [79]. The initial reaction involves oxidation due to photogenerated holes, while the subsequent reaction involves reduction stemming from photogenerated electrons. Initially, in the ground state, all electrons occupy the valence band (VB). Upon exposure to light of the appropriate wavelength, electrons are energised to the conduction band (CB), creating a positive hole (h⁺) in the VB and a negative electron (e[−]) in the CB [80]. Therefore, the presence of carbon nanospheres (CSs) aids in trapping the photoinduced electrons, extending their lifespan and promoting the separation of charge carriers [81]. Additionally, CSs exhibit significant absorption of organic species, contributing to the effective degradation of organic pollutants. Simultaneously, the incorporation of silver (Ag)/gold (Au) into the ZnO framework proves to be an effective strategy, primarily attributed to its surface Plasmon resonance (SPR) property [40,82]. This property induces the oscillation of free electrons at the interface between Ag/Au and the ZnO host, leading to a shift in optical absorption towards longer wavelengths within

the visible region [41,83]. In the photocatalysis process, these charge carriers (h^+ and e^-) play a pivotal role in degrading methylene blue (MB) dye through their interaction with oxygen (e^-) and water (h^+), producing superoxide ($O_2^{\cdot-}$) and hydroxide ($\cdot OH$) ions. These ions then react with the MB dye, facilitating its degradation into various intermediates (Figure S2) and eventually into H_2O and CO_2 .



Scheme 2. Photodegradation mechanism of MB by 1% Ag-ZnO-CSs and 1% Au-ZnO-CSs.

Effects of various conditions on photocatalytic activity of MB

The 20/80 ZnO-CSs nanocomposite was utilised to check the optimum photodegradation conditions that would be used for the study. Notably, ZnO-CSs demonstrated an enhanced surface area of $21.95 \text{ m}^2/\text{g}$ compared to the $11.07 \text{ m}^2/\text{g}$ surface area of green-synthesised ZnO-NPs detailed in our previous study [47]. The superior photocatalytic properties of 20/80 ZnO-CSs prompted further investigation into optimisation experiments. In this section, optimisation of pH, dosage, and dye concentration was explored using the 20/80 ZnO-CSs. Various pH levels (3, 5, 7, and 10), dosage amounts (15, 30, 45, and 90 mg), and dye concentrations (5, 10, 15, and 20 mg/L) were examined, with the optimal conditions identified as pH 5, a dosage of 90 mg of photocatalyst, and a dye concentration of 5 mg/L.

pH Influence

The pH level plays an essential role in removal efficiency by influencing the adsorption chemistry between the adsorbent and adsorbate [9]. Maximum degradation percentages observed at pH 3, 5, 7, and 10 are 13%, 42%, 40%, and 35%, respectively (refer to Figure 6a,b). Consequently, pH 5 was selected for further investigation. This pH-dependent removal

mechanism can be attributed to variations in electrostatic attraction between the surface of ZnO–CSs and the dye MB. Optimal electrostatic attraction at pH 5 leads to enhanced pollutant degradation compared to pH 3, where the driving force is stronger [15]. At pH 10, the surface charge of ZnO–CSs becomes positive [21], resulting in decreased degradation of anions on ZnO–CSs in an aqueous environment. Since methylene blue has a pKa of 3.8, cationic species dominate the solution for pH values above this threshold [22], leading to higher concentrations of the anionic form of MB at pH greater than pKa. The degradation of MB by ZnO–CSs was found to be higher at the natural pH of MB, which is pH 5 in this study. Additionally, the oxidation potential of hydroxyl radicals decreases with increasing pH, resulting in reduced dye degradation at pH values above 5 [24]. Moreover, the elevated concentration of OH ions in the solution leads to competition between OH ions and the anionic form of MB, consequently decreasing MB degradation by ZnO–CSs nanocomposites [25].

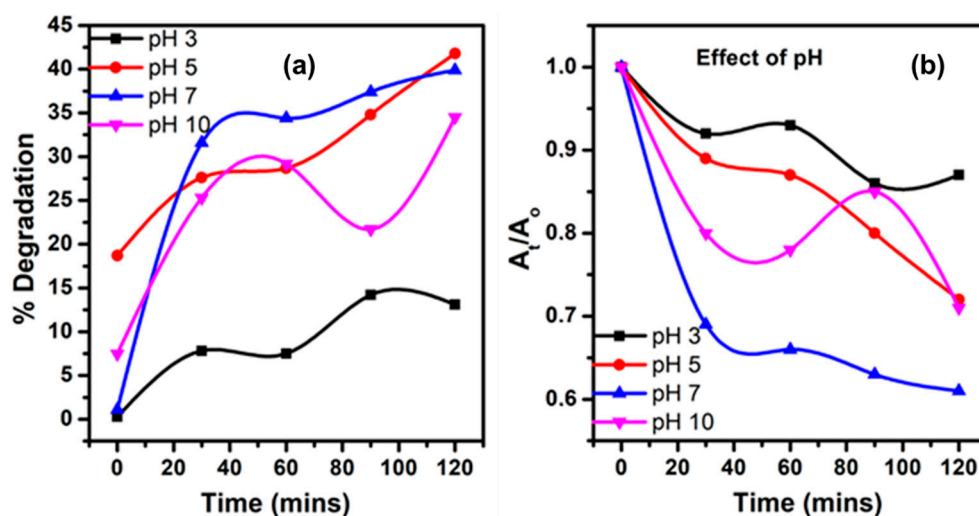


Figure 6. Degradation efficiency of ZnO–CSs (20/80) against MB (a) represented by % degradation and (b) A_t/A_0 plots on various pH.

Influence of ZnO–CSs dose

To examine the impact of the dosage of the 20/80 ZnO–CSs photocatalyst on the degradation of MB, varying amounts of catalyst (15, 30, 45, and 90 mg) were introduced into the solution under consistent conditions, including a reaction time of 120 min, pH 5, and an initial MB concentration of 20 mg/L. The UV-Vis curves illustrating the outcomes of these analyses are presented in Figure 7a,b. The corresponding degradation percentages for 15, 30, 45, and 90 mg were 10%, 42%, 34%, and 64%, respectively.

Figure 7a,b indicates no degradation when 15 mg of the catalyst was employed. However, an increase in the catalyst amount to 30 mg resulted in a noticeable 42% degradation of MB. At a dosage of 45 mg, degradation was measured at 34%, while at 90 mg, the degradation efficiency reached 64% [9]. This can be attributed to the heightened availability of surface-active sites with an increased catalyst amount, leading to an augmented production of hydroxyl radicals and, consequently, enhanced photocatalytic activity of ZnO–CSs. Excessive catalyst concentration, however, can impede UV light penetration into the catalyst surface, limiting the generation of hydroxyl radicals and reducing dye degradation efficiency [15,26]. Consequently, a photocatalyst dosage of 90 mg was selected for further investigation.

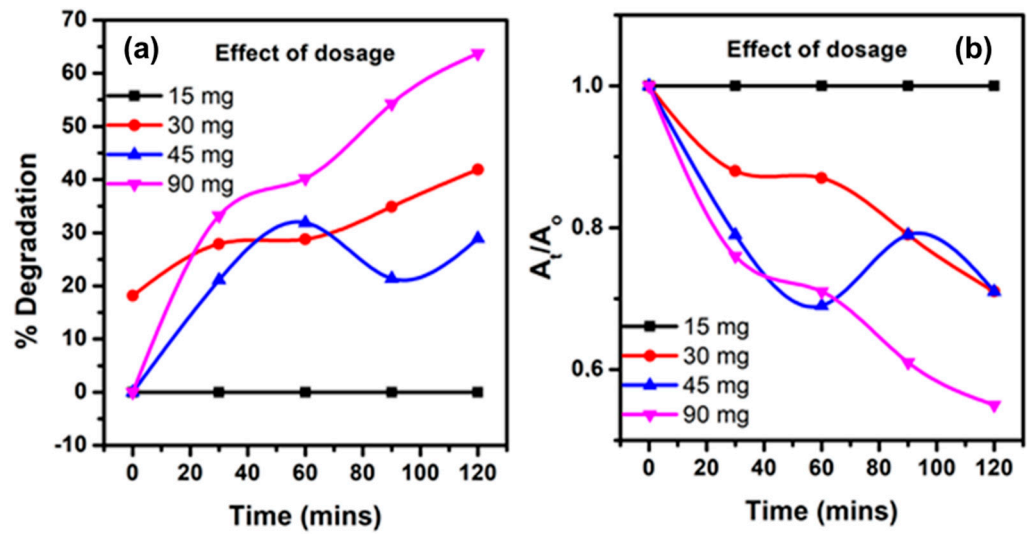


Figure 7. Degradation efficiency of ZnO–CSs (20/80) against MB (a) represented by % degradation and (b) A_t/A_0 plots at 15, 30, 45, and 90 mg.

Influence of MB Concentration

The highest degradation percentages observed at concentrations of 5, 10, 15, and 20 mg/L were 75%, 63%, 43%, and 42%, respectively. The Figure 8a,b illustrates these findings. The results indicate that increasing the initial dye concentration resulted in reduced degradation. This phenomenon could be attributed to a decrease in the number of available surface-active sites, consequently leading to a reduction in hydroxyl radical production and subsequent photocatalytic activity. Furthermore, elevated dye concentrations shortened the path length of photons entering the dye solution. At higher dye concentrations, the dye molecules may absorb a significant portion of solar light instead of the catalyst, thereby diminishing catalytic efficiency [27,84]. Therefore, in this investigation, it was essential to work with a higher concentration of MB solution (20 mg/L) to enhance the catalytic capabilities of the materials.

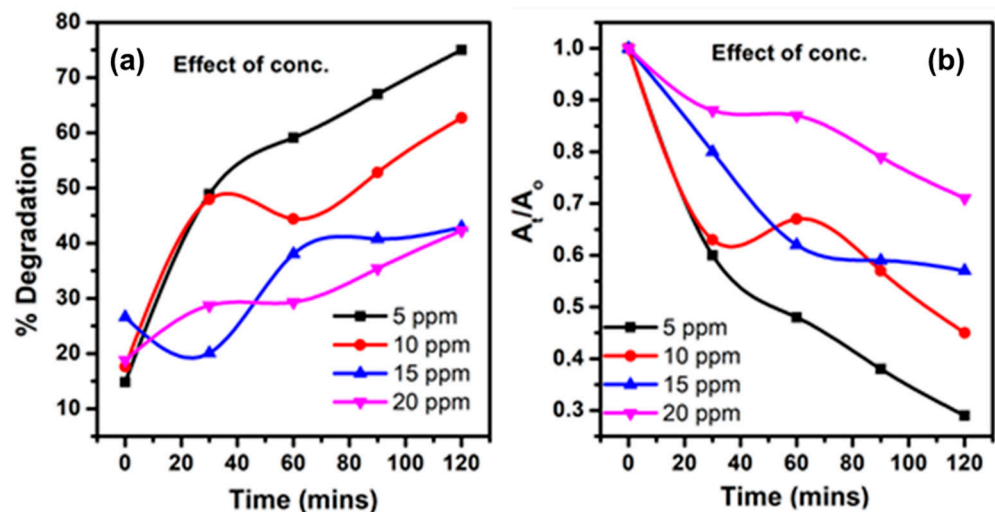


Figure 8. Degradation efficiency of ZnO–CSs (20/80) against MB (a) represented by % degradation and (b) A_t/A_0 plots at 5–20 mg/L dye solution.

Furthermore, the results from the UV-vis photodegradation curves (Figure 9a–d) show the degradation of MB by 20/80 ZnO–CSs, 1% Ag–ZnO–CSs, and 1% Au–ZnO–CSs nanocomposites using the 5 ppm MB concentration at pH 5 and 90 mg dosage of photocatalyst over 120 min.

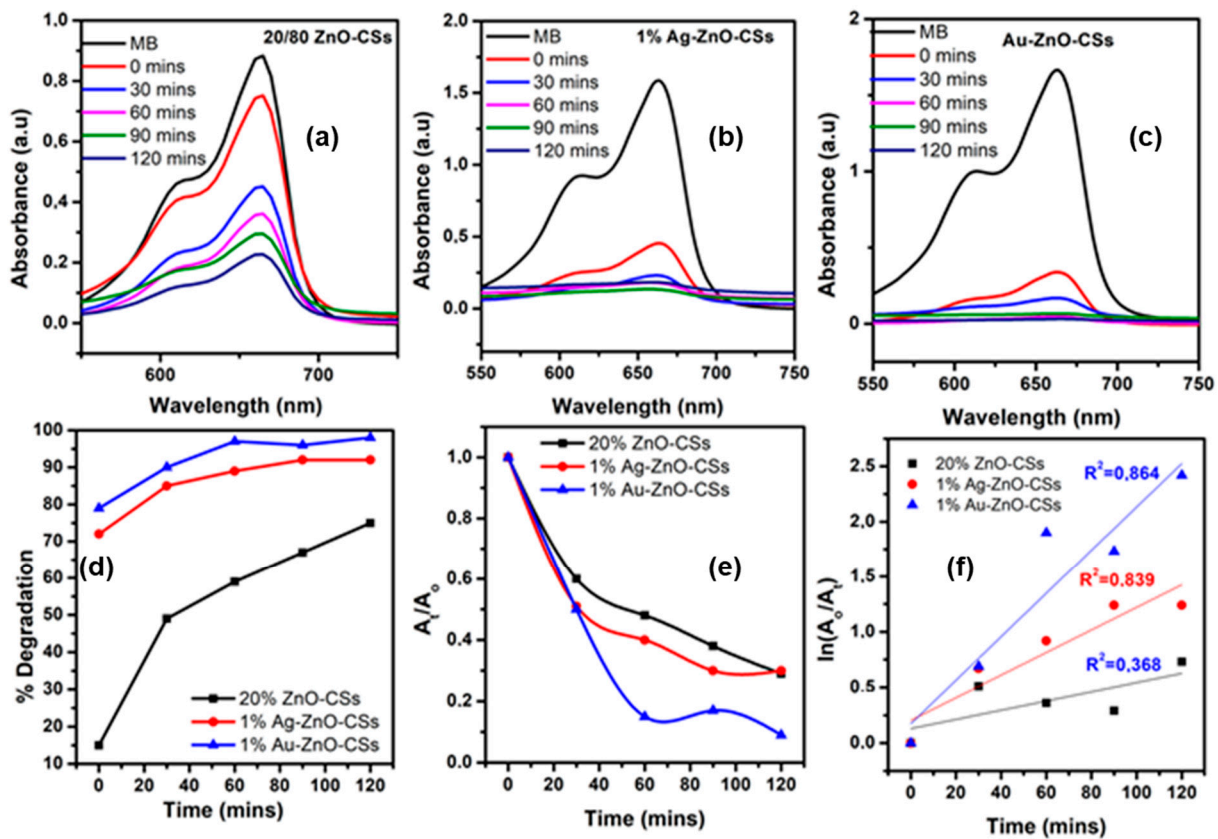


Figure 9. UV-Vis diagrams representing degradation of MB by (a) 20/80 ZnO-CSs, (b) 1% Ag-ZnO-CSs, (c) 1% Au-ZnO-CSs, and the (d) degradation efficiencies, (e) A_t/A_0 plots, and (f) kinetics of 20/80 ZnO-CSs, 1%Ag-ZnO-CSs, and 1% Au-ZnO-CSs.

The highest degradation rates (Figure 9c,d) of 75%, 92%, and 98% for the 20/80 ZnO-CSs, 1% Ag-ZnO-CSs, and 1% Au-ZnO-CSs, respectively, were found. The synthesised 20/80 ZnO-CSs, 1% Ag-ZnO-CSs, and 1% Au-ZnO-CSs nanocomposite did not achieve the first order of kinetics because the R^2 was not closer to 1. The reaction rates of 20/80 ZnO-CSs, 1% Ag-ZnO-CSs, and 1% Au-ZnO-CSs were 0.00368, 0.01017, and 0.00196, respectively.

Research indicates that the addition of carbon spheres (CSs) enhances the photocatalytic activity of ZnO-CSs under sunlight and visible light irradiation. This improvement is attributed to the extended light absorption range of CSs and their ability to rapidly separate photogenerated charge carriers [85]. Additionally, the presence of CSs facilitates the dispersion of ZnO-C in the methylene blue (MB) solution due to their lightweight nature. In the case of 1% Ag-ZnO-CSs, the silver nanoparticles (Ag NPs) contribute to harvesting visible light energy for ZnO through their surface Plasmon resonance (SPR) effect. Moreover, they enhance the separation of photogenerated charge carriers by serving as an electron reservoir. As a result, 1% Ag-ZnO-CSs exhibit higher efficiency in degrading under sunlight and visible light compared to ZnO alone. The combined effects of CSs and Ag NPs lead to increased light absorption intensity and enhanced efficiency in separating photogenerated charge carriers for 1% Ag-ZnO-CSs. One possible explanation for these higher degradation rates is that the noble metal-doped ZnO-NPs enhance the photocatalytic efficiency in the UV region of the light spectrum, since all the materials exhibited a maximum absorbance band in the UV spectrum. The maximum absorbance band of ZnO-CSs was found to be 300.7 nm with a shoulder around 287.5 nm, while the maximum absorbance band of 1% Ag-ZnO-CSs was 298 nm with a shoulder band at 286 nm and the 1% Au-ZnO-CSs had a maximum absorbance band around 290 nm, though it is expected that the absorbance should be moving towards the visible region instead of

moving backwards to the UV region. The findings of this study are almost comparable to those of other studies published in the literature where UV, visible, and sunlight light sources were used to degrade organic materials using similar nanocomposites (see Table 2).

Table 2. Various studies of the degradation of dyes metal-doped ZnO–CSs nanocomposites.

Photocatalyst	Light Source	Dye	Time (min)	Conc. (mg/L)	Volume of Solution (mL)	Dosage	Efficiency (%)	Refs
ZnO@C	Visible	RBG	120	10	NR	30 mg	~95.8	[73]
Ag/ZnO@C	Sunlight	RhB	40	10	NR	100	~97.9	[40]
1% Ag/ZnO	UV	MB	80	10	NR	24 mg	57	[85]
Au–ZnO	UV	MB	60	10	NR	20 mg	50	[82]
Au/ZnO	UV	ORII	180	10	400	1.5 g/L	87.4	[41]
1% Ag–ZnO–CSs	UV	MB	120	5	300	90 mg	92	[current study]
1% Au–ZnO–CSs	UV	MB	120	5	300	90 mg	98	[current study]

RBG = Reactive Black GR, RhB = Rhodamine B, MB = Methylene blue, ORII = Orange II. NR: Not reported.

Furthermore, research indicates that the addition of carbon spheres (CSs) enhances the photocatalytic activity of ZnO–CSs under sunlight and visible light irradiation. This improvement is attributed to the extended light absorption range of CSs and their ability to rapidly separate photogenerated charge carriers [85]. Additionally, the presence of CSs facilitates the dispersion of ZnO–C in the methylene blue (MB) solution due to their lightweight nature. In the case of 1% Ag–ZnO–CSs, the silver nanoparticles (Ag NPs) contribute to harvesting visible light energy for ZnO through their surface Plasmon resonance (SPR) effect. Moreover, they enhance the separation of photogenerated charge carriers by serving as an electron reservoir [86]. As a result, 1% Ag–ZnO–CSs exhibit higher efficiency in degrading under sunlight and visible light compared to ZnO alone. The combined effects of CSs and Ag NPs lead to increased light absorption intensity and enhanced efficiency in separating photogenerated charge carriers for 1% Ag–ZnO–CSs. In these studies, it can be noted that the presence of carbon and AgO synergistically work together for trapping and increasing the surface area to benefit more active sites on the material, thus optimisation in our study might be of importance. It is important to note that the light source used plays a major role. Though the degradation rates were very high as compared to the previously reported studies, the primary purpose of this work was to enhance the properties of these materials, such that they would be active in the visible light region, and they were still active in the UV region.

The 1% Au–ZnO–CSs were found to be the best nanocomposites amongst the three materials; hence, it has been used further for reusability studies, trapping studies as well as the degradation of pharmaceuticals. It is worth noting that the higher degradation was also reported for the pharmaceuticals, and it is important to understand whether the material is stable, as stability and efficiency are both characteristics that make it the best material for photocatalytic applications.

3.7.1. Reusability Studies

The reusability studies for four cycles using the 1% Au–ZnO–CSs are shown in Figure 10a–c, with a 2 h UV light exposure duration, for each cycle. The catalyst was not stable as the degradation was reduced from the 1st cycle by more than 50%. After the 4th cycle, a complete collapse in the degradation took place. To test the efficiency of the 1% Au–ZnO/C against other pollutants, this material was tested against various pharmaceutical pollutants.

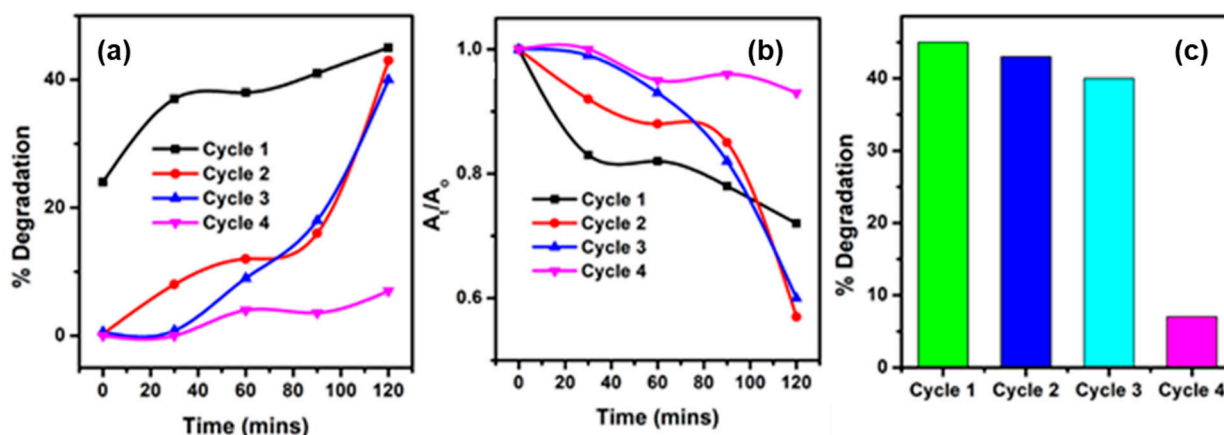


Figure 10. (a–c) Degradation efficiency for cycles 1 to 4 for the 1% Au–ZnO–CSs.

3.7.2. MB Trapping Studies

To understand the photodegradation mechanism of MB utilizing the 1% Au–ZnO–CSs nanocomposite, a series of experiments were conducted employing iso-propyl alcohol (IPA, 5 mmol L⁻¹), EDTA (5 mmol L⁻¹), AgNO₃ (5 mmol L⁻¹), and p-benzoquinone (BQ, 5 mmol L⁻¹) as scavengers for hole (h⁺), hydroxyl radical (OH•), electron (e⁻), and superoxide (•O₂²⁻), respectively. As depicted in Figure 11, all scavengers employed in these investigations influenced the degradation rate of MB. Notably, the inclusion of AgNO₃ significantly decreased the degradation rate, followed by IPA addition. On the other hand, the introduction of EDTA and BQ slightly decreased the MB degradation rate. These findings highlight the extensive involvement of both OH• radicals and the e⁻ in the MB photodegradation, thereby confirming that the existence of Au and CSs plays a crucial role in trapping photoinduced electrons and induces free electron oscillation in the photodegradation process [80,82].

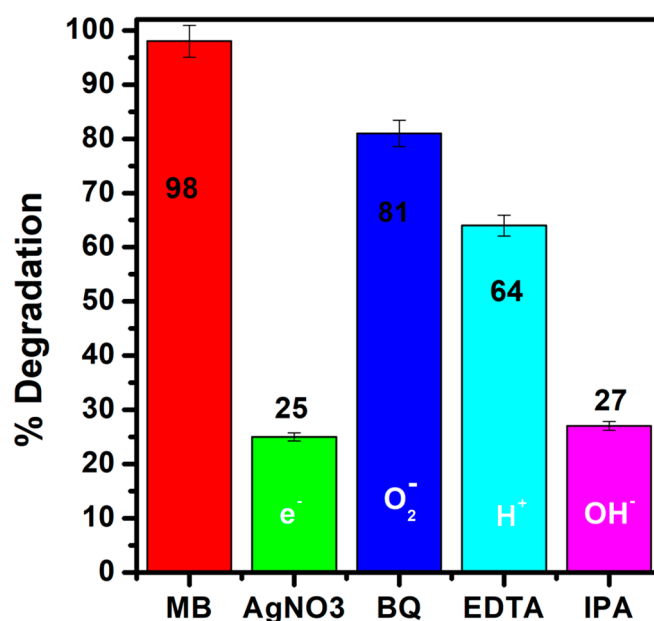


Figure 11. Effect of scavengers on the photocatalytic degradation of MB by 1% Au–ZnO–CSs.

3.7.3. Photodegradation of Various Pharmaceuticals

The degradation of pharmaceuticals (CBZ, CIP, SMX, and SSX), were conducted by using 100 mg photocatalyst and 10 mg/L concentration of contaminant (Figure 12). Similar conditions as with MB were followed for the 1% Ag–ZnO–CSs photocatalyst, which

degraded about 96% (SSX), 89% (CIP), 78% (SMX), and 29% (CBZ). The photodegradation curves in Figure S3 further show the degradation efficiency of the pharmaceuticals. This means that the 1% Au-ZnO-CSs is the best photocatalyst, which can degrade various contaminants. The incorporation of the 20/80 ZnO-CSs with 1% Ag and 1% Au increased the degradation of MB (at optimised conditions) to be 90% and 98%, respectively.

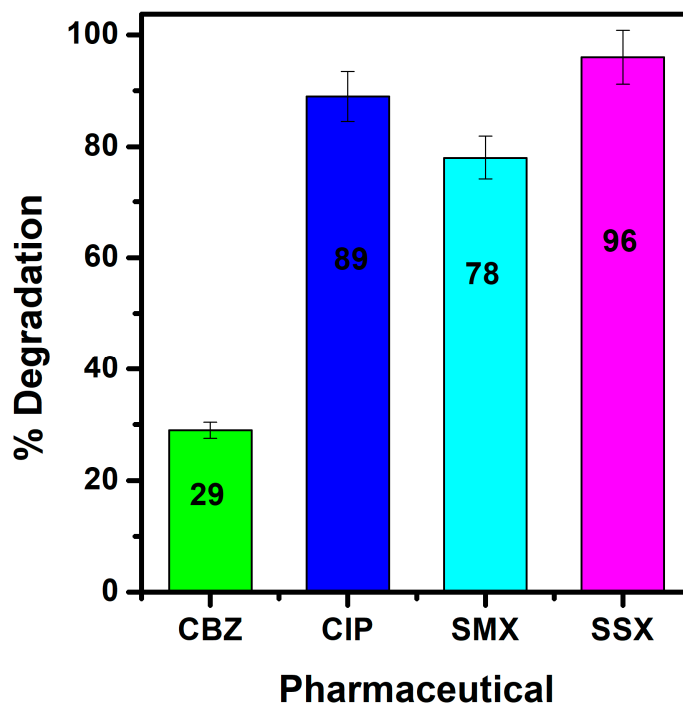


Figure 12. Percentage degradation diagrams of CBZ, CIP, SMX, and SSX by 1% Au-ZnO-CSs.

4. Conclusions

In this study, the spherically shaped materials (1% Ag-ZnO-CSs and 1% Au-ZnO-CSs) with various particle sizes were successfully synthesised. A maximum absorbance peak around 290 nm for the 1% Ag-ZnO-CSs and 1% Au-ZnO-CSs, respectively, was noted. Moreover, the addition of these noble metals influenced the material to be more active in the UV region. TGA reported a decrease in stability for 1% Ag-ZnO-CSs and 1% Au-ZnO-CSs as the total weight loss was reported to be ~65% and ~70%, while for the 20/80 ZnO-CSs it was 46%. Under optimised conditions, the 1% Au-ZnO-CSs showed the highest degradation of MB, which was 98%, while the 1% Ag-ZnO-CSs and the 20/80 ZnO-CSs degraded 92% and 75% of the textile dye, respectively. The most active species in the degradation process of MB by the 1% Au-ZnO-CSs were found to be the hydroxide radicals as well as the electrons. The reusability studies showed that on the fourth cycle, the degradation efficiency of the material completely dropped to less than 5%. The material degraded 96% (SSX), 89% (CIP), 78% (SMX), and 29% (CBZ). This study showed that the 1% Au-ZnO-CSs is a flexible photo catalyst, which can be used to degrade various dyes and pharmaceuticals.

Supplementary Materials: The following supporting information can be downloaded at: <https://www.mdpi.com/article/10.3390/textiles4010008/s1>, Figure S1: EDS mapping for (a) 1% Ag-ZnO-CSs, (b) 1% Au-ZnO-CSs and (c) 20/80 ZnO-CSs; Figure S2: The photocatalytic degradation mechanism of the MB dye; Figure S3: Photodegradation Curves for (a) CBZ, (b) CIP, (c) SMX and (d) SSX by the 1% Au-ZnO-CSs photocatalyst.

Author Contributions: Conceptualization, N.C.H.-M. and D.E.M.; methodology, D.A.B.; formal analysis, D.A.B.; resources, N.C.H.-M. and D.E.M.; writing—original draft preparation, D.A.B.;

writing—review and editing, N.C.H.-M.; supervision, N.C.H.-M. and D.E.M.; funding acquisition, N.C.H.-M. and D.E.M. All authors have read and agreed to the published version of the manuscript.

Funding: This research received support from the DSI-NRF CoE in Strong Materials (R808) and the NRF Thuthuka grant (UID 117999) to cover operational expenses. We also extend gratitude to NRF Sasol Inzalo for providing student funding.

Data Availability Statement: Data are contained within the article and supplementary materials.

Acknowledgments: We acknowledge the chemistry department at the University of Limpopo for granting access to laboratory facilities.

Conflicts of Interest: The authors declare no conflict of interest.

References

1. Mallikarjunaswamy, C.; Lakshmi Ranganatha, V.; Ramu, R.; Udayabhanu; Nagaraju, G. Facile microwave-assisted green synthesis of ZnO nanoparticles: Application to photodegradation, antibacterial and antioxidant. *J. Mater. Sci. Mater. Electron.* **2020**, *31*, 1004–1021. [[CrossRef](#)]
2. Otieno, F.A.; Ochieng, G.M. Water management tools as a means of averting a possible water scarcity in South Africa by the year 2025. *Water SA* **2004**, *30*, 120–124. [[CrossRef](#)]
3. Arismendi, D.; Becerra-Herrera, M.; Cerrato, I.; Richter, P. Simultaneous determination of multiresidue and multiclass emerging contaminants in waters by rotating-disk sorptive extraction–derivatization-gas chromatography/mass spectrometry. *Talanta* **2019**, *201*, 480–489. [[CrossRef](#)]
4. Basha, C.A.; Chithra, E.; Sripriyalakshmi, N.K. Electro-degradation and biological oxidation of non-biodegradable organic contaminants. *Chem. Eng. J.* **2009**, *149*, 25–34. [[CrossRef](#)]
5. Suresh, D.; Nethravathi, P.C.; Rajanaika, H.; Nagabhushana, H.; Sharma, S.C. Green synthesis of multifunctional zinc oxide (ZnO) nanoparticles using Cassia fistula plant extract and their photodegradative, antioxidant and antibacterial activities. *Mater. Sci. Semicond. Process.* **2015**, *31*, 446–454. [[CrossRef](#)]
6. Sharma, A.; Nagraik, R.; Sharma, S.; Sharma, G.; Pandey, S.; Azizov, S.; Chauhan, P.K.; Kumar, D. Green synthesis of ZnO nanoparticles using Ficus palmata: Antioxidant, antibacterial and antidiabetic studies. *Results Chem.* **2022**, *4*, 100509. [[CrossRef](#)]
7. Arami, M.; Limaee, N.Y.; Mahmoodi, N.M.; Tabrizi, N.S. Removal of dyes from colored textile wastewater by orange peel adsorbent: Equilibrium and kinetic studies. *J. Colloid Interface Sci.* **2005**, *288*, 371–376. [[CrossRef](#)]
8. Ratnamala, G.M.; Shetty, K.V.; Srinikethan, G. Removal of remazol brilliant blue dye from dye-contaminated water by adsorption using red mud: Equilibrium, kinetic, and thermodynamic studies. *Water Air Soil Pollut.* **2012**, *223*, 6187–6199. [[CrossRef](#)]
9. Nasrollahzadeh, M.S.; Hadavifar, M.; Ghasemi, S.S.; Arab Chamjangali, M. Synthesis of ZnO nanostructure using activated carbon for photocatalytic degradation of methyl orange from aqueous solutions. *Appl. Water Sci.* **2018**, *8*, 104. [[CrossRef](#)]
10. Kang, S.; Zhao, Y.; Wang, W.; Zhang, T.; Chen, T.; Yi, H.; Rao, F.; Song, S. Removal of methylene blue from water with montmorillonite nanosheets/chitosan hydrogels as adsorbent. *Appl. Surf. Sci.* **2018**, *448*, 203–211. [[CrossRef](#)]
11. Uddin, M.T.; Islam, M.A.; Mahmud, S.; Rukanuzzaman, M. Adsorptive removal of methylene blue by tea waste. *J. Hazard. Mater.* **2009**, *164*, 53–60. [[CrossRef](#)] [[PubMed](#)]
12. Bayomie, O.S.; Kandeel, H.; Shoeib, T.; Yang, H.; Youssef, N.; El-Sayed, M.M. Novel approach for effective removal of methylene blue dye from water using fava bean peel waste. *Sci. Rep.* **2020**, *10*, 7824. [[CrossRef](#)]
13. Wainwright, M.; Crossley, K.B. Methylene blue—a therapeutic dye for all seasons? *J. Chemother.* **2002**, *14*, 431–443. [[CrossRef](#)] [[PubMed](#)]
14. Mashkooor, F.; Nasar, A. Magsorbents: Potential candidates in wastewater treatment technology—A review on the removal of methylene blue dye. *J. Magn. Magn. Mater.* **2020**, *500*, 166408. [[CrossRef](#)]
15. Noorimotlagh, Z.; Darvishi Cheshmeh Soltani, R.; Shams Khorramabadi, G.; Godini, H.; Almasian, M. Performance of wastewater sludge modified with zinc oxide nanoparticles in the removal of methylene blue from aqueous solutions. *Desalination Water Treat.* **2016**, *57*, 1684–1692. [[CrossRef](#)]
16. Semeraro, P.; Comparelli, R. Application of photocatalysts in Environmental Chemistry. *Catalysts* **2024**, *14*, 174. [[CrossRef](#)]
17. Mazeo, N.; Marzi, D.; Bavasso, I.; Piemonte, V. Removal of Methylene Blue from Wastewater by Waste Roots from the Arsenic-Hyperaccumulator *Pteris vittata*: Fixed Bed Adsorption Kinetics. *Materials* **2023**, *16*, 1450. [[CrossRef](#)]
18. Calisto, V.; Domingues, M.R.M.; Erny, G.L.; Esteves, V.I. Direct photodegradation of carbamazepine followed by micellar electrokinetic chromatography and mass spectrometry. *Water Res.* **2011**, *45*, 1095–1104. [[CrossRef](#)]
19. Lam, M.W.; Mabury, S.A. Photodegradation of the pharmaceuticals atorvastatin, carbamazepine, levofloxacin, and sulfamethoxazole in natural waters. *Aquat. Sci.* **2005**, *67*, 177–188. [[CrossRef](#)]
20. Fu, H.; Gray, K.A. TiO₂ (Core)/Crumpled Graphene Oxide (Shell) Nanocomposites Show Enhanced Photodegradation of Carbamazepine. *Nanomaterials* **2021**, *11*, 2087. [[CrossRef](#)]
21. Daneshvar, N.; Aber, S.; Dorraji, M.S.; Khataee, A.R.; Rasoulifard, M.H. Photocatalytic degradation of the insecticide diazinon in the presence of prepared nanocrystalline ZnO powders under irradiation of UV-C light. *Sep. Purif. Technol.* **2007**, *58*, 91–98. [[CrossRef](#)]

22. Sousa, H.R.; Silva, L.S.; Sousa, P.A.A.; Sousa, R.R.M.; Fonseca, M.G.; Osajima, J.A.; Silva-Filho, E.C. Evaluation of methylene blue removal by plasma activated palygorskites. *J. Mater. Res. Technol.* **2019**, *8*, 5432–5442. [[CrossRef](#)]
23. Dutta, S.; Gupta, B.; Srivastava, S.K.; Gupta, A.K. Recent Advances on the removal of dyes from wastewater using various adsorbents: A critical review. *Mater. Adv.* **2021**, *2*, 4497–4531. [[CrossRef](#)]
24. Lucas, M.S.; Peres, J.A. Decolorization of the azo dye Reactive Black 5 by Fenton and photo-Fenton oxidation. *Dye. Pigment.* **2006**, *71*, 236–244. [[CrossRef](#)]
25. Saini, J.; Garg, V.K.; Gupta, R.K.; Kataria, N. Removal of Orange G and Rhodamine B dyes from aqueous system using hydrothermally synthesized zinc oxide loaded activated carbon (ZnO-AC). *J. Environ. Chem. Eng.* **2017**, *5*, 884–892. [[CrossRef](#)]
26. Mills, A.; Davies, R.H.; Worsley, D. Water purification by semiconductor photocatalysis. *Chem. Soc. Rev.* **1993**, *22*, 417–425. [[CrossRef](#)]
27. Rao, A.N.; Sivasankar, B.; Sadasivam, V. Kinetic study on the photocatalytic degradation of salicylic acid using ZnO catalyst. *J. Hazard. Mater.* **2009**, *166*, 1357–1361.
28. Abellán, M.N.; Bayarri, B.; Giménez, J.; Costa, J.J.A.C.B.E. Photocatalytic degradation of sulfamethoxazole in aqueous suspension of TiO₂. *Appl. Catal. B Environ.* **2007**, *74*, 233–241. [[CrossRef](#)]
29. Mahlaule-Glory, L.M.; Hintsho-Mbita, N.C. Green Derived Zinc Oxide (ZnO) for the Degradation of Dyes from Wastewater and Their Antimicrobial Activity: A Review. *Catalysts* **2022**, *12*, 833. [[CrossRef](#)]
30. Quek, J.A.; Sin, J.C.; Lam, S.M.; Mohamed, A.R.; Zeng, H. Bioinspired green synthesis of ZnO structures with enhanced visible light photocatalytic activity. *J. Mater. Sci. Mater. Electron.* **2020**, *31*, 1144–1158. [[CrossRef](#)]
31. Kumar, V.; Gohain, M.; Som, S.; Kumar, V.; Bezuindenhoudt, B.C.B.; Swart, H.C. Microwave assisted synthesis of ZnO nanoparticles for lighting and dye removal application. *Phys. B Condens. Matter* **2016**, *480*, 36–41. [[CrossRef](#)]
32. Li, Y.; Xie, W.; Hu, X.; Shen, G.; Zhou, X.; Xiang, Y.; Zhao, X.; Fang, P. Comparison of dye photodegradation and its coupling with light-to-electricity conversion over TiO₂ and ZnO. *Langmuir* **2010**, *26*, 591–597. [[CrossRef](#)]
33. Ibrahim, J.; Ajaegbu, V.C.; Egharevba, H.O. Pharmacognostic and phytochemical analysis of *Commelina benghalensis* L. *Ethnobot. Leaflet*. **2010**, *2010*, 7.
34. Grover, I.S.; Prajapat, R.C.; Singh, S.; Pal, B. Highly photoactive Au-TiO₂ nanowires for improved photo-degradation of propiconazole fungicide under UV/sunlight irradiation. *Sol. Energy* **2017**, *144*, 612–618. [[CrossRef](#)]
35. Deshmukh, A.A.; Mhlanga, S.D.; Coville, N.J. Carbon spheres. *Mater. Sci. Eng. R Rep.* **2010**, *70*, 1–28. [[CrossRef](#)]
36. Iijima, S. Helical microtubules of graphitic carbon. *Nature* **1991**, *354*, 56–58. [[CrossRef](#)]
37. Arumugam, M.; Manikandan, D.B.; Dhandapani, E.; Sridhar, A.; Balakrishnan, K.; Markandan, M.; Ramasamy, T. Green synthesis of zinc oxide nanoparticles (ZnO NPs) using *Syzygium cumini*: Potential multifaceted applications on antioxidants, cytotoxic and as nanonutrient for the growth of *Sesamum indicum*. *Environ. Technol. Innov.* **2021**, *23*, 101653. [[CrossRef](#)]
38. Anitha, J.; Selvakumar, R.; Hema, S.; Murugan, K.; Premkumar, T. Facile green synthesis of nano-sized ZnO using leaf extract of *Morinda tinctoria*: MCF-7 cell cycle arrest, antiproliferation, and apoptosis studies. *J. Ind. Eng. Chem.* **2022**, *105*, 520–529. [[CrossRef](#)]
39. Alshabanat, M.N.; AL-Anazy, M.M. An experimental study of photocatalytic degradation of congo red using polymer nanocomposite films. *J. Chem.* **2018**, *2018*, 9651850. [[CrossRef](#)]
40. Niu, B.; Wu, D.; Wang, J.; Wang, L.; Zhang, W. Salt-sealing-pyrolysis derived Ag/ZnO@C hollow structures towards efficient photo-oxidation of organic dye and water-born bacteria. *Appl. Surf. Sci.* **2020**, *528*, 146965. [[CrossRef](#)]
41. Chen, P.K.; Lee, G.J.; Davies, S.H.; Masten, S.J.; Amutha, R.; Wu, J.J. Hydrothermal synthesis of coral-like Au/ZnO catalyst and photocatalytic degradation of Orange II dye. *Mater. Res. Bull.* **2013**, *48*, 2375–2382. [[CrossRef](#)]
42. Ngoepe, N.M.; Mathipa, M.M.; Hintsho-Mbita, N.C. Biosynthesis of titanium dioxide nanoparticles for the photodegradation of dyes and removal of bacteria. *Optik* **2020**, *224*, 165728. [[CrossRef](#)]
43. Munyai, S.; Mahlaule-Glory, L.M.; Hintsho-Mbita, N.C. Green Synthesis of Zinc Sulphide (ZnS) nanostructures using *S.frutescence* plant extract for photocatalytic degradation of dyes and antibiotics. *Mater. Res. Express* **2022**, *9*, 015001. [[CrossRef](#)]
44. Zwane, B.N.; Mabuba, N.; Orimolade, B.O.; Koiki, B.A.; Arotiba, O.A. Photocatalytic degradation of ciprofloxacin and sulfamethoxazole on a carbon nanodot doped tungsten trioxide: Degradation product study. *React. Kinet. Mech. Catal.* **2020**, *131*, 453–470. [[CrossRef](#)]
45. Bashir, B.; Shaheen, W.; Asghar, M.; Warsi, M.F.; Khan, M.A.; Haider, S.; Shakir, I.; Shahid, M. Copper doped manganese ferrites nanoparticles anchored on graphene nano-sheets for high performance energy storage applications. *J. Alloys Compd.* **2017**, *695*, 881–887. [[CrossRef](#)]
46. Atarod, M.; Nasrollahzadeh, M.; Sajadi, S.M. Euphorbia heterophylla leaf extract mediated green synthesis of Ag/TiO₂ nanocomposite and investigation of its excellent catalytic activity for reduction of variety of dyes in water. *J. Colloid Interface Sci.* **2016**, *462*, 272–279. [[CrossRef](#)]
47. Bopape, D.A.; Motaung, D.E.; Hintsho-Mbita, N.C. Green synthesis of ZnO: Effect of plant concentration on the morphology, optical properties and photodegradation of dyes and antibiotics in wastewater. *Optik* **2022**, *251*, 168459. [[CrossRef](#)]
48. Nagaraju, G.; Prashanth, S.A.; Shastri, M.; Yathish, K.V.; Anupama, C.; Rangappa, D. Electrochemical heavy metal detection, photocatalytic, photoluminescence, biodiesel production and antibacterial activities of Ag-ZnO nanomaterial. *Mater. Res. Bull.* **2017**, *94*, 54–63. [[CrossRef](#)]

49. Dou, P.; Tan, F.; Wang, W.; Sarreshteh, A.; Qiao, X.; Qiu, X.; Chen, J. One-step microwave-assisted synthesis of Ag/ZnO/graphene nanocomposites with enhanced photocatalytic activity. *J. Photochem. Photobiol. A Chem.* **2015**, *302*, 17–22. [[CrossRef](#)]
50. Rajbongshi, B.M.; Ramchiary, A.; Jha, B.M.; Samdarshi, S.K. Synthesis and characterization of plasmonic visible active Ag/ZnO photocatalyst. *J. Mater. Sci. Mater. Electron.* **2014**, *25*, 2969–2973. [[CrossRef](#)]
51. Sapkota, K.P.; Lee, I.; Hanif, M.A.; Islam, M.A.; Hahn, J.R. Solar-light-driven efficient ZnO–single-walled carbon nanotube photocatalyst for the degradation of a persistent water pollutant organic dye. *Catalysts* **2019**, *9*, 498. [[CrossRef](#)]
52. Yu, Z.; Zhang, L.; Wang, X.; He, D.; Suo, H.; Zhao, C. Fabrication of ZnO/Carbon quantum dots composite sensor for detecting NO gas. *Sensors* **2020**, *20*, 4961. [[CrossRef](#)] [[PubMed](#)]
53. Du, Y.; Zhao, F.; Liu, L.; Gao, Y.; Xing, L.; Li, Q.; Fu, C.; Zhong, Z.; Zhang, X. Improvement of bond strength between ZnO nanorods and carbon fibers using magnetron sputtered ZnO films as the interphase. *CrystEngComm* **2017**, *19*, 868–875. [[CrossRef](#)]
54. Saoud, K.; Alsoubaihi, R.; Bensalah, N.; Bora, T.; Bertino, M.; Dutta, J. Synthesis of supported silver nano-spheres on zinc oxide nanorods for visible light photocatalytic applications. *Mater. Res. Bull.* **2015**, *63*, 134–140. [[CrossRef](#)]
55. Xu, S.; Zhang, H.; Qi, L.; Xiao, L. Conductometric acetone vapor sensor based on the use of gold-doped three-dimensional hierarchical porous zinc oxide microspheres. *Microchim. Acta* **2019**, *186*, 342. [[CrossRef](#)]
56. Yang, S.; Wang, L.; Yan, Y.; Yang, L.; Li, X.; Lu, Z.; Zhai, H.; Han, D.; Huo, P. Two hybrid Au-ZnO heterostructures with different hierarchical structures: Towards highly efficient photocatalysts. *Sci. Rep.* **2019**, *9*, 16863. [[CrossRef](#)]
57. Majhi, S.M.; Rai, P.; Yu, Y.T. Facile approach to synthesize Au@ZnO core-shell nanoparticles and their application for highly sensitive and selective gas sensors. *ACS Appl. Mater. Interfaces* **2015**, *7*, 9462–9468. [[CrossRef](#)]
58. Kadam, A.N.; Bhopate, D.P.; Kondalkar, V.V.; Majhi, S.M.; Bathula, C.D.; Tran, A.V.; Lee, S.W. Facile synthesis of Ag-ZnO core-shell nanostructures with enhanced photocatalytic activity. *J. Ind. Eng. Chem.* **2018**, *61*, 78–86. [[CrossRef](#)]
59. Kotlhaio, K.; Mtunzi, F.M.; Pakade, V.; Laloo, N.; Ejidike, I.P.; Modise, S.J.; Moutloali, R.M.; Klink, M.J. Enhancing the photocatalytic degradation of selected chlorophenols using Ag/zno nanocomposites. *MRS Adv.* **2018**, *3*, 2129–2136. [[CrossRef](#)]
60. Patil, S.S.; Patil, R.H.; Kale, S.B.; Tamboli, M.S.; Ambekar, J.D.; Gade, W.N.; Kolekar, S.S.; Kale, B.B. Nanostructured microspheres of silver@zinc oxide: An excellent impeder of bacterial growth and biofilm. *J. Nanoparticle Res.* **2014**, *16*, 1–11. [[CrossRef](#)]
61. Tran Thi, V.H.; Pham, T.N.; Pham, T.T.; Le, M.C. Synergistic adsorption and photocatalytic activity under visible irradiation using Ag-ZnO/GO nanoparticles derived at low temperature. *J. Chem.* **2019**, *2019*, 2979517. [[CrossRef](#)]
62. Bopape, D.A.; Mathobela, S.; Matinise, N.; Motaung, D.E.; Hintsho-Mbita, N.C. Green synthesis of CuO-TiO₂ for the degradation of organic pollutants: Physical, Optical and Electrochemical Properties. *Catalyst* **2023**, *13*, 163. [[CrossRef](#)]
63. Fageria, P.; Gangopadhyay, S.; Pande, S. Synthesis of ZnO/Au and ZnO/Ag nanoparticles and their photocatalytic application using UV and visible light. *Rsc Adv.* **2014**, *4*, 24962–24972. [[CrossRef](#)]
64. Gogurla, N.; Sinha, A.K.; Santra, S.; Manna, S.; Ray, S.K. Multifunctional Au-ZnO plasmonic nanostructures for enhanced UV photodetector and room temperature NO sensing devices. *Sci. Rep.* **2014**, *4*, 6483. [[CrossRef](#)]
65. Liu, L.; Yang, H.; Ren, X.; Tang, J.; Li, Y.; Zhang, X.; Cheng, Z. Au-ZnO hybrid nanoparticles exhibiting strong charge-transfer-induced SERS for recyclable SERS-active substrates. *Nanoscale* **2015**, *7*, 5147–5151. [[CrossRef](#)] [[PubMed](#)]
66. Chang, Q.Q.; Cui, Y.W.; Zhang, H.H.; Chang, F.; Zhu, B.H.; Yu, S.Y. C-doped ZnO decorated with Au nanoparticles constructed from the metal-organic framework ZIF-8 for photodegradation of organic dyes. *RSC Adv.* **2019**, *9*, 12689–12695. [[CrossRef](#)]
67. Poinern, G.E.J.; Brundavanam, S.; Shah, M.; Laava, I.; Fawcett, D. Photothermal response of CVD synthesized carbon (nano) spheres/aqueous nanofluids for potential application in direct solar absorption collectors: A preliminary investigation. *Nanotechnol. Sci. Appl.* **2012**, *5*, 49. [[CrossRef](#)] [[PubMed](#)]
68. Kayani, Z.N.; Manzoor, F.; Zafar, A.; Mahmood, M.; Rasheed, M.; Anwar, M. Impact of Ag doping on structural, optical, morphological, optical and photoluminescent properties of ZnO nanoparticles. *Opt. Quantum Electron.* **2020**, *52*, 1–18. [[CrossRef](#)]
69. Langa, C.; Hintsho-Mbita, N.C. Plant and bacteria mediated synthesis of TiO₂ NPs for dye degradation in water. A review. *Chem. Phys. Imp.* **2023**, *7*, 100293. [[CrossRef](#)]
70. Ramesan, M.T.; Siji, C.; Kalaprasad, G.; Bahuleyan, B.K.; Al-Maghrabi, M.A. Effect of silver doped zinc oxide as nanofiller for the development of biopolymer nanocomposites from chitin and cashew gum. *J. Polym. Environ.* **2018**, *26*, 2983–2991. [[CrossRef](#)]
71. Kaur, A.; Ibhaden, A.O.; Kansal, S.K. Photocatalytic degradation of ketorolac tromethamine (KTC) using Ag-doped ZnO microplates. *J. Mater. Sci.* **2017**, *52*, 5256–5267. [[CrossRef](#)]
72. Bonyani, M.; Zebarjad, S.M.; Janghorban, K.; Kim, J.Y.; Kim, H.W.; Kim, S.S. Au-Decorated Polyaniline-ZnO Electrospun Composite Nanofiber Gas Sensors with Enhanced Response to NO₂ Gas. *Chemosensors* **2022**, *10*, 388. [[CrossRef](#)]
73. Patil, S.S.; Mali, M.G.; Tamboli, M.S.; Patil, D.R.; Kulkarni, M.V.; Yoon, H.; Kim, H.; Al-Deyab, S.S.; Yoon, S.S.; Kolekar, S.S.; et al. Green approach for hierarchical nanostructured Ag-ZnO and their photocatalytic performance under sunlight. *Catal. Today* **2016**, *260*, 126–134. [[CrossRef](#)]
74. Kot, M.; Wojcieszak, R.; Janiszewska, E.; Pietrowski, M.; Zieliński, M. Effect of modification of amorphous silica with ammonium agents on the physicochemical properties and hydrogenation activity of Ir/SiO₂ catalysts. *Materials* **2021**, *14*, 968. [[CrossRef](#)] [[PubMed](#)]
75. Cychosz, K.A.; Thommes, M. Progress in the physisorption characterization of nanoporous gas storage materials. *Engineering* **2018**, *4*, 559–566. [[CrossRef](#)]
76. Tijani, J.O.; Fatoba, O.O.; Totito, T.C.; Roos, W.D.; Petrik, L. Synthesis and characterization of carbon doped TiO₂ photocatalysts supported on stainless steel mesh by sol-gel method. *Carbon Lett.* **2017**, *22*, 48–59.

77. Pandey, M.; Singh, M.; Wasnik, K.; Gupta, S.; Patra, S.; Gupta, P.S.; Pareek, D.; Chaitanya, N.S.N.; Maity, S.; Reddy, A.B.; et al. Targeted and enhanced antimicrobial inhibition of mesoporous ZnO–Ag₂O/Ag, ZnO–CuO, and ZnO–SnO₂ composite nanoparticles. *ACS Omega* **2021**, *6*, 31615–31631. [[CrossRef](#)]
78. Wang, Z.; Jiang, X.; Pan, M.; Shi, Y. Nano-scale pore structure and its multi-fractal characteristics of tight sandstone by n₂ adsorption/desorption analyses: A case study of shihezi formation from the sulige gas field, ordos basin, china. *Minerals* **2020**, *10*, 377. [[CrossRef](#)]
79. Sillanpää, M.; Matilainen, A. NOM removal by advanced oxidation processes. In *Natural Organic Matter in Water: Characterization and Treatment Methods*; Butterworth-Heinemann: Oxford, UK, 2015; pp. 159–211.
80. Jiang, C.; Zhang, W.; Zou, G.; Yu, W.; Qian, Y. Precursor-induced hydrothermal synthesis of flowerlike cupped-end microrod bundles of ZnO. *J. Phys. Chem. B* **2005**, *109*, 1361–1363. [[CrossRef](#)]
81. Ahmad, M.; Ahmad, I.; Ahmed, E.; Akhtar, M.S.; Khalid, N.R. Facile and inexpensive synthesis of Ag doped ZnO/CNTs composite: Study on the efficient photocatalytic activity and photocatalytic mechanism. *J. Mol. Liq.* **2020**, *311*, 113326. [[CrossRef](#)]
82. Pawinrat, P.; Mekasuwandumrong, O.; Panpranot, J. Synthesis of Au–ZnO and Pt–ZnO nanocomposites by one-step flame spray pyrolysis and its application for photocatalytic degradation of dyes. *Catal. Commun.* **2009**, *10*, 1380–1385. [[CrossRef](#)]
83. Zhao, X.; Su, S.; Wu, G.; Li, C.; Qin, Z.; Lou, X.; Zhou, J. Facile synthesis of the flower-like ternary heterostructure of Ag/ZnO encapsulating carbon spheres with enhanced photocatalytic performance. *Appl. Surf. Sci.* **2017**, *406*, 254–264. [[CrossRef](#)]
84. Sobana, N.; Muruganandam, M.; Swaminathan, M. Characterization of AC–ZnO catalyst and its photocatalytic activity on 4-acetylphenol degradation. *Catal. Commun.* **2008**, *9*, 262–268. [[CrossRef](#)]
85. Sharma, J.; Sharma, S.; Soni, V. Classification and impact of synthetic textile dyes on Aquatic Flora: A review. *Reg. Stud. Mar. Sci.* **2021**, *45*, 101802. [[CrossRef](#)]
86. Singh, S. Natural sunlight driven photocatalytic performance of Ag/ZnO nanocrystals. *Mater. Today Commun.* **2022**, *33*, 104438. [[CrossRef](#)]

Disclaimer/Publisher’s Note: The statements, opinions and data contained in all publications are solely those of the individual author(s) and contributor(s) and not of MDPI and/or the editor(s). MDPI and/or the editor(s) disclaim responsibility for any injury to people or property resulting from any ideas, methods, instructions or products referred to in the content.